Improving the representation of dust and water cycles in the UK Mars GCM

David Mulholland

First Year Report

Atmospheric, Oceanic and Planetary Physics
Department of Physics
University of Oxford

Supervisors: Prof. Peter Read
& Dr. Stephen Lewis

August 2009

Contents

Chapter 1

Introduction

The greatly-increased number of spacecraft missions in the past decade, together with ongoing refinement of climate modelling techniques, make Mars the most actively-studied and accurately-modelled planet besides our own. Mars general circulation models (GCMs) are now of comparable sophistication to terrestrial climate models, and the recent influx of new observational data makes constraining and improving these models a high priority, in order to assist our understanding of the on-site data that are obtained. In addition, model predictions are an integral part of future mission planning.

The UK Mars GCM, based partly at Oxford University, accurately represents the key dynamics behind the Martian climate, and replicates the temperature and pressure structure of the atmosphere, as well as the large-scale wind-flow patterns. Recent work done on the code saw the addition of physical schemes to model dust particle lifting and transport (a vital component in determining atmospheric temperature on Mars) and to simulate water sublimation and condensation in the atmosphere, on the ground, and below the surface.

Currently, however, the two 'tracer' (dust and water) schemes are not designed to run simultaneously. It is therefore an initial aim of my project to reconfigure the UKMGCM code to allow both dust and water to be transported at the same time. The longer-term goal is to couple the two schemes together, to have changes in one field affect the subsequent behaviour of the other.

The principal mechanism by which this interaction is believed to occur on Mars is the nucleation of cloud ice particles around a dust aerosol core. This has the twin effects of promoting water ice cloud formation (by means of heterogeneous nucleation) as well as hastening the removal from the atmosphere of the dust particle (due to its increased settling rate inside a heavy ice shell).

Such 'scavenging' interactions may exert a significant influence on climate through their effect on atmospheric dust opacity. Ice covering increases a dust particle's albedo, while the more rapid sedimentation induced acts to limit the dust particle distribution in the vertical. The resultant cooling is expected to be non-linear, due to the relationship between vapour amount and atmospheric saturation height, and feedbacks associated with the change in availability of

cloud nucleation centres. The idea behind developing a model for these interactions is then to assess what thermodynamic effect dust scavenging has on the atmosphere, and in what regions and seasons it becomes most important.

Dust/water interactions may also be of importance when studying climates from recent Martian history, in particular due to the varying dust fractions thought to have been sedimented along with water ice at the poles, under certain orbital conditions, to form the so-called polar layered deposits. With this in mind, a short study has been carried out to investigate the effect of changes in orbital parameters (such as the planetary obliquity) on the Martian water cycle. An adapted version of the current UKMGCM, transporting water only, was used for these experiments. It is hoped that the simulations can be returned to at a later date, with a more detailed model capable of representing both dust and water physics, as well as interaction between the two.

The structure of my report is then as follows:

Chapter 2 reviews the current knowledge of the modern Martian climate system, with regard in particular to the water and dust cycles. Chapter 3 then explains the basic ideas behind differences in climate that are believed to apply in previous Martian eras, and describes some of the outstanding issues which GCM studies (like the one undertaken here or, more realistically, that which will become possible by the end of this project) can hope to address in the near future.

The key features of the UK Mars General Circulation Model are outlined in Chapter 4, which also includes mention of some of the limitations of the model, and the improvements that it is hoped will be made within the duration of this project.

Chapters 5 and 6 then describe the work undertaken this year to run the series of 'past climate' experiments. Chapter 5 concerns the setting up of a usable water-transporting code, the modifications that have been made to the original water scheme, and the simulations that were carried out. Comment is also made on the current model representation of the Martian water cycle, and how this can be improved. Chapter 6 relates some of the results obtained from the study, and points towards refinements that may be possible in the near future.

Finally, Chapter 7 presents a plan of work to be done for the remainder of the project, in order to produce a model code capable of modelling dust and water side-by-side, as well as simulating some aspect of their interaction.

Chapter 2

The present Martian climate

2.1 Circulation

The low heat capacity of the thin Martian atmosphere means that diurnal and seasonal temperature variations are large [Leovy, 2001]. In summer, surface temperature typically reaches around 260 K, with winter polar regions experiencing lows of ∼140 K — this is below the freezing point of carbon dioxide, the principal atmospheric constituent, which therefore condenses to form seasonal polar caps. As much as a third of the atmospheric mass is exchanged with the surface over the course of a year, with greater amounts of deposition occurring at the south pole [Litvak et al., 2005], on account of the longer and colder southern winter season (currently occurring when the planet is at aphelion).

At the solstices, the Martian circulation is dominated by a strong and asymmetric Hadley cell, extending between north and south mid-latitudes, producing trade winds and allowing cross-equatorial transport of dust, water and other species. The cell shifts northward in northern winter, with an ascending branch south of the equator, northward flow up to heights of 50 km or more, and a descending branch in the northern tropics [Leovy, 2001]. The flow direction reverses in southern winter, but the cell is strongest and widest in northern winter (due to the coincidence of this season with perihelion), giving a flow annually biased towards the northern hemisphere.

A condensation flow, directed towards the winter pole, occurs due to the freezing out of atmospheric carbon dioxide onto the winter cap, and eddy transports also contribute in the polar regions. In winter and spring seasons in both hemispheres, baroclinic and/or barotropic instabilities in the zonal wind and temperature structure at high latitudes set up an eastward-travelling planetary wave flow, with zonal wavenumbers of one to three. Baroclinic eddies are more prevalent in the northern hemisphere, while both hemispheres are baroclinically stable in their respective summertimes [Read and Lewis, 2004].

During the daytime a convective zone is set up in the lower portion of the atmosphere, known as the planetary boundary layer (PBL). Convection allows the atmosphere to become well-mixed up to the top of the PBL, which extends approximately 3–10 km (up to one atmospheric scale height) above the surface, depending on season [Hinson et al., 2008]. In this way the PBL regulates the exchange of dust and water between the surface and the upper, stably stratified, atmosphere. From observations by the Mars Express mission, Hinson et al. [2008] found that the convective boundary layer has its greatest vertical extent above elevated terrain, but is much shallower over low-lying regions. At nighttime the boundary layer is much shallower and more stable.

Martian topography is a significant factor in its atmospheric dynamics. Several of its mountains, most notably Olympus Mons, reach heights of more than 20 km above the 'areoid' (the geopotential reference level on Mars), much higher than any point on Earth, and importantly more than the Martian atmospheric scale height. Large surface height changes such as these influence atmospheric circulation by generating stationary planetary waves as winds pass over, as well as the physical blocking effect that they exert on wind flow [Read and Lewis, 2004]. Such wave structures have been observed in Martian temperature profiles, for example using Mars Global Surveyor data by Hinson et al. [2001].

Notably, most of the southern hemisphere sits higher than northern regions, by several kilometres on average [Zuber et al., 2000]. The reasons for this hemispheric dichotomy are thought to trace back to the formation period of the planet, over 3.5 Gyr ago [Read and Lewis, 2004]. This cross-equatorial sloping affects atmospheric transport, adding to the northern winter Hadley cell's dominance of the annual circulation pattern. In fact Richardson and Wilson [2002] suggested that topography may be more important than the timing of perihelion or any other effect in biasing the annual-mean cross-equatorial transport.

2.2 Water

Compared to Earth, the atmosphere of Mars is extremely dry, containing on average only a few precipitable microns of water (meaning that if the entire water column at any point were condensed down to the surface, it would form a layer much less than one millimetre deep). Atmospheric vapour, cloud formation, and exchange with the surface and subsurface nonetheless make up an important part of the Martian climate. Current knowledge of the water cycle is summarised below.

2.2.1 Atmospheric vapour

Since the first detection of water vapour on Mars, by Spinrad et al. [1963], mapping of the atmospheric humidity has been performed both via Earth-based observations, with orbiting satellites and on the Martian surface. Dating back to the Viking missions in the seventies, the principal atmospheric vapour data for many years was that obtained by the Viking Orbiter Mars Atmospheric

Water Detectors (MAWD) [Jakosky and Farmer, 1982]. MAWD data showed a maximum column abundance of 90 prμm at the north pole in northern summer, near $L_s = 120°$, with a much weaker maximum during southern summer of around 15 prμm at the south pole. Away from the poles over much of the year, the vapour column was seen to be around 10 prμm. These findings differed somewhat from previous measurements by Barker et al. [1970], which indicated a wetter southern spring and summer, with a maximum of around 40prμm.

Mars Global Surveyor, which arrived at Mars in 1999, carried on board the Thermal Emission Spectrometer (TES), spectra from which allowed a close examination of water vapour over a full Martian year [Smith, 2002] (see Figure 2.1). A large maximum near the north pole was seen at $L_s = 110°$–$120°$, with vapour abundance falling away moving southward. Northern hemisphere water abundance then declined into autumn and winter, except for a sustained 20 prμm 'tongue' at northern low latitudes, which extended towards northern winter. The southern hemisphere maximum was measured at $\sim$40 prμm poleward of 75°S at $L_s = 290°$ — larger than MAWD observed, and peaking slightly later. Concurrent with the southern summer maximum was a smaller local maximum in the northern hemisphere, at the tail end of the low latitude tongue, which is a feature not observed in the corresponding southern hemispheric location during northern summer. Reanalysis of MAWD data, to adjust for shielding of the vapour signal by large dust amounts, brought the results largely in line with TES [Fedorova et al., 2004].

Most recent measurements have come from Mars Express, carrying the Planetary Fourier Spectrometer (PFS) [Formisano et al., 2005]. Results from the long-wavelength PFS channel [Fouchet et al., 2007] suggested a generally drier water cycle than had been found by TES — in particular, a reduced north polar maximum of less than 60 prμm was noted. In light of these results, the TES dataset was reanalysed and found to be biased towards high column values when using certain wavelength bands. After this correction was applied to the TES results they were found to be largely in line with the PFS data [Fouchet et al., 2007]. An amount of variation still exists between the many datasets, from both space- and Earth-based observations (e.g. [Sprague et al., 2006, Titov et al., 1999]) perhaps partly due to real interannual variability, which occurs primarily in perihelion season [Smith, 2004].

The vertical distribution of water vapour on Mars is not yet well-known, though limited measurements (e.g. [Rodin et al., 1997]) do exist. Both PFS/LW and TES measurements suggested that the water column is not well-mixed [Fouchet et al., 2007, Smith, 2002], and Tschimmel et al. [2008] also found evidence that vapour is to some extent confined to lower levels of the column. They suggest this is due to a slower vertical mixing above the PBL, combined with a comparatively rapid supply to low levels by the surface and/or subsurface (see 2.2.3, 2.2.4).

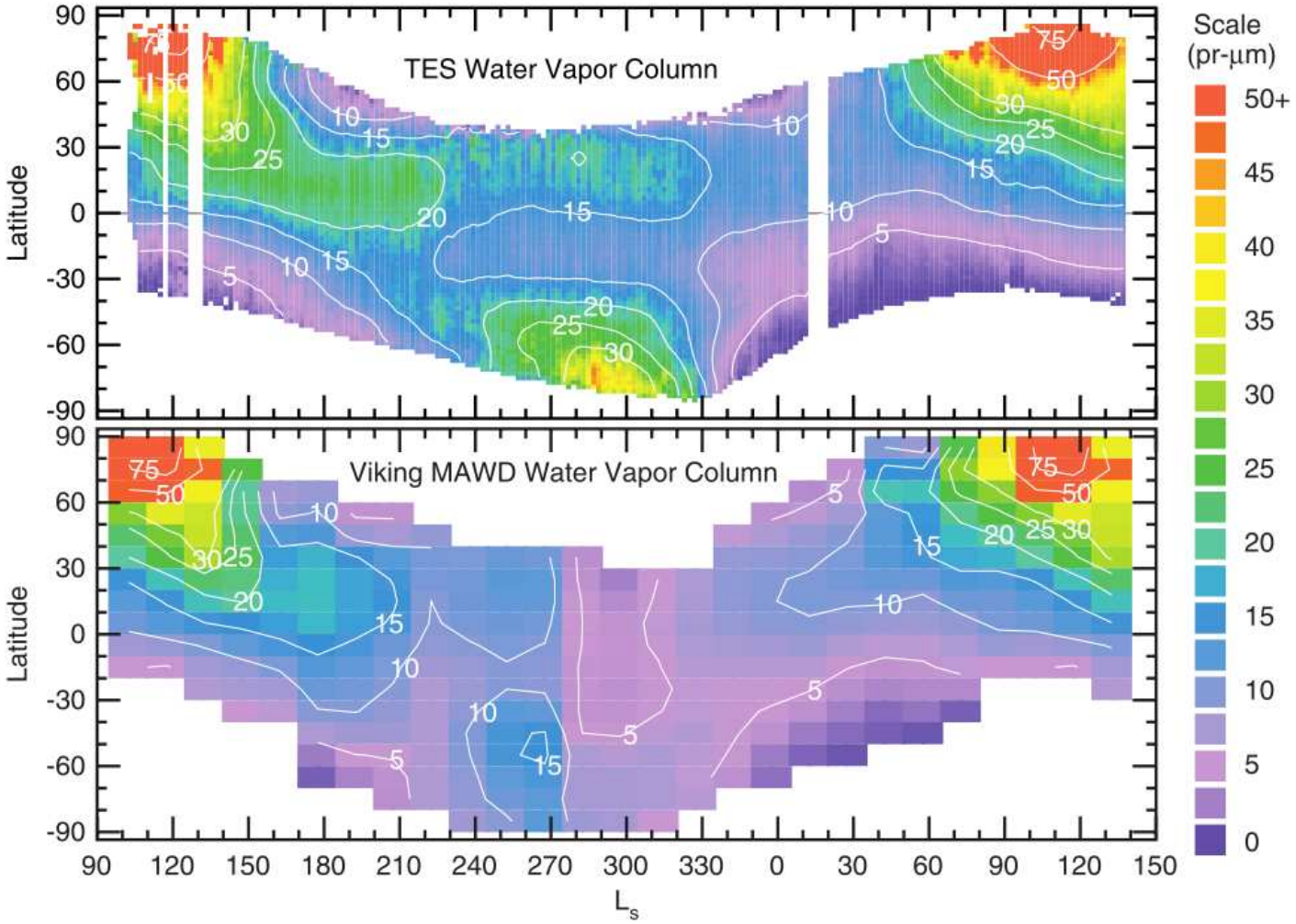

Figure 2.1: Annual water vapour column abundances as seen by TES (before the downward correction) and MAWD. From Smith [2002].

2.2.2 Clouds

Water ice clouds can form in the Martian atmosphere whenever local pressure falls below the saturation vapour pressure for the amount of water present, causing vapour to condense and form ice particles, typically of radii 1–4 μm [Wolff and Clancy, 2003, Zasova et al., 2005], though larger cloud particles can be found at low altitudes [Whiteway et al., 2009]. The most prominent ice cloud regions are an equatorial belt around aphelion, and 'polar hood' clouds at the edges of the polar caps [Smith, 2004]. Low clouds often form at night as the atmospheric temperature drops, and persist through the morning until temperature rises sufficiently again. Coagulation of particles to form a precipitable mass is unlikely, and so ice crystals settle slowly under gravity, with most subliming at a lower, warmer level, rather than reaching the surface as ice [Jakosky, 1985]. The LIDAR on the Phoenix Lander [Whiteway et al., 2009] observed fall streaks in the boundary layer region which are interpreted (in line with what is seen on Earth) as precipitation occurring. Dust particles in the atmosphere may act as nucleation centres for water ice and thus enhance cloud formation.

Clouds radiate heat efficiently in the thermal infrared and thus have a cooling effect on the surrounding atmosphere. Their presence has therefore been given [Colaprete and Toon, 2000] as the explanation for inversions in temperature (cooler close to the surface) observed in the lower layers of the atmosphere by, for example, the Mars Pathfinder lander [Magalhães et al., 1999] (Figure 2.2). These inversions can be of magnitude 10–15 K, and may be caused by clouds with a visible opacity of as little as $\sim$0.1, which commonly form at night.

Condensation height is found to have a strong dependence on temperature, with heights of 10–20 km during northern hemisphere summer, but greater than 40 km near perihelion, when increased dust opacity and solar flux give rise to higher atmospheric temperatures [Smith, 2002]. The TES data illustrate well the two distinct seasonal climates of present-day Mars — a cool and cloudy aphelion season, and a warm, dusty and cloud-free perihelion season.

Clancy et al. [1996] highlighted a link between condensation height at aphelion and cross-equatorial vapour transport, as occurs via the solstice Hadley cell circulation. As ice crystals are removed from the atmosphere (by gravity) much more quickly than the vapour phase, the condensation height effectively caps the vapour column, which in the cool aphelion season prevents water from reaching the upper part of the Hadley cell. In the warmer perihelion (southern summer) season, however, condensation occurs higher in the atmosphere, so water vapour can more readily be advected by the Hadley circulation, particularly at mid-latitudes where meridional transport takes place at greater altitudes. This so-called 'Clancy effect' therefore produces greater vapour transport into the northern hemisphere in southern summer than in the return direction during northern summer. Combined with the fact that circulation is stronger at perihelion, this leads to a south-north vapour pump, offering an explanation for the asymmetry in vapour abundance between the two hemispheres.

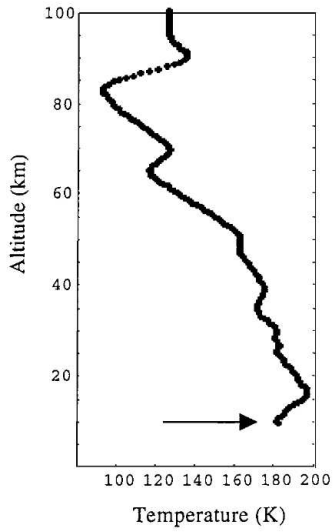

Figure 2.2: Mars Pathfinder vertical temperature profile, with the inversion below 20 km probably due to the presence of a water ice cloud (from Colaprete and Toon [2000]).

2.2.3 The polar caps

The large increase in water vapour abundance (to a global maximum) at northern high latitudes in late spring and early summer suggests that a key source is the receding seasonal north polar ice cap [Smith, 2002]. The northern hemisphere possesses a residual (permanent) water ice cap underneath the seasonal CO_2 deposits [Kieffer et al., 1976, Feldman et al., 2003], which is revealed when the CO_2 sublimes off in summer, allowing water ice sublimation. The north polar cap covers an area of 10^6 km^2 with a thickness of up to a few km [Zuber et al., 1998], with seasonal CO_2 deposition increasing elevation by up to a metre at high latitudes and peaking in late winter [Smith et al., 2001].

At the south pole however, the CO_2 cap is present all year round, never fully subliming away, perhaps due to the cooler surface temperatures allowed by higher elevation (around 6 km) at the south pole relative to that at the north, or a higher cap albedo. Nonetheless areas of water ice a few km wide have been observed at the retreating edge of the CO_2 cap [Titus et al., 2003], so if the cap can on occasion disappear entirely [Barker et al., 1970, Jakosky and Haberle, 1990], a residual water ice sheet could have formed under the south polar cap as well.

Visible at both poles is a striping pattern (first observed by the Mariner 9 spacecraft [Murray et al., 1972]), revealed by troughs along the sloped face of the cap, showing that the polar caps have a layered structure in the vertical. Pairs of dark and bright layers are 10–30 m thick [Milkovich and Head, 2005].

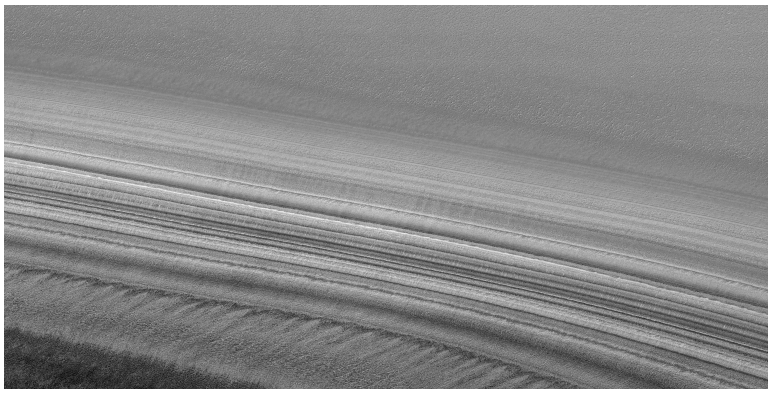

Figure 2.3: A Mars Global Surveyor image of the northern polar layered deposits. Image credit: NASA/JPL/University of Arizona

These 'polar layered deposits' (PLD) (Figure 2.3) have varying albedo which is believed to be due to differing dust contents within the ice; the atmospheric dust having been deposited onto the cap along with the water ice, possibly as nucleation cores for ice crystals (see 2.3.2, and later 3.2.2).

2.2.4 Subsurface deposits

It has been suggested by Haberle and Jakosky [1990] that sublimation from the residual northern water ice cap alone may not provide all the water required to create the observed north polar maximum, and indeed that vapour sublimed from the cap would not be adequately transported equatorwards by the polar circulation to replicate (MAWD) observations southwards of about 75°. An additional source for the vapour seen in northern hemisphere summer may then be the Martian subsurface, known as the regolith. The upper portion of the ground layer on Mars is somewhat porous, made up of loose-fitting rock and sand, and water vapour can seep into this 'soil', where it may then become adsorbed to the soil grains, or freeze out to form ice deposits. On daily timescales water can diffuse a metre or less below the surface, but on much longer timescales it may penetrate down to depths of several km, a region often called the 'megaregolith' [Read and Lewis, 2004].

Zent et al. [1993] used a one-dimensional model to simulate exchange between the regolith and lower atmosphere. They estimated that the subsurface (containing adsorbed water) could come into equilibrium with a dry atmosphere within about 15 sols (Martian solar days), with most of the vapour being supplied within the first two sols, suggesting that the regolith can buffer the atmospheric vapour column on a daily timescale. The study found that the regolith acts as both a source and a sink to the atmosphere at different times of day, with typically 5% of the vapour column exchanged diurnally.

The Gamma Ray Spectrometer on Mars Odyssey was used to detect amounts of hydrogen in the upper metre of the regolith, and this, in correlation with

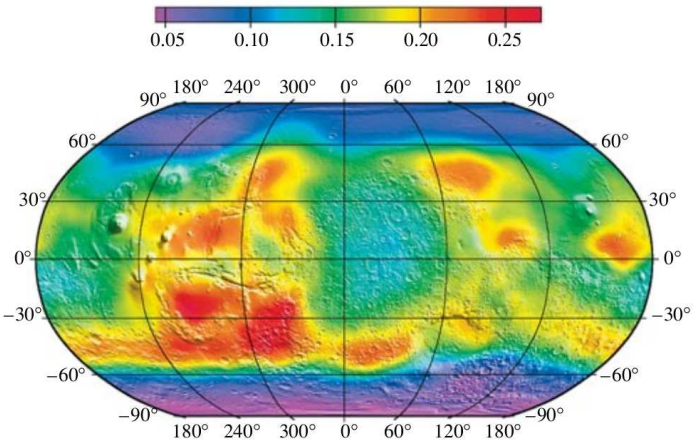

Figure 2.4: Mars Odyssey High Energy Neutron Detector results (neutron flux in counts per second) from Mitrofanov et al. [2004]. Low neutron flux denotes regions of high subsurface hydrogen concentration, which are found most obviously at the poles, with some subsurface ice also detected in equatorial regions, correlated with regions of low thermal inertia.

predicted regions of ice stability [Farmer and Doms, 1979], was interpreted as being in the form of water ice, mixed with some rock or soil material [Boynton et al., 2002]. Significant ice deposits, representing as much as 50% of the regolith layer by mass, are present at both poles, overlain by a dry soil layer of thickness 10–20 cm at southern high latitudes (with the layer thickness increasing from pole to mid-latitudes) but situated close to the surface (with no dry layer) at northern high latitudes [Litvak et al., 2006]. The proximity of water to the surface near the north pole suggests that regolith desorption can indeed contribute to the increase in humidity in northern spring and summer.

2.3 Atmospheric dust

The Martian atmosphere contains a suspension of dust particles, typically of radius 1–2 μm (or larger) [Read and Lewis, 2004]. These particles are composed of a combination of clay, basalt and silicate materials swept up from the surface topsoil into the atmospheric circulation [Toon et al., 1977].

Baseline visible opacity due to dust is around 0.2, observed in the clearer aphelion season, but in southern summer the initiation of global dust storms can lift large amounts of dust into the atmosphere and cause opacities in excess of unity. Extinction due to dust is assumed to be around twice as strong in the optical (0.67 μm) as the infrared (9 μm) [Forget, 1998], so the presence of an atmospheric dust layer has the effect of warming the atmosphere close to the dust, while having a net cooling effect on the surface during daytime hours

and a warming influence at night – basically, reducing the diurnal temperature variation near the surface, by shielding it from the changes in solar insolation between day and night.

Zasova et al. [2005], using PFS data from a Mars Express orbit, observed a strong anti-correlation between dust opacity and surface height, and deduced that opacity decreased exponentially with altitude with a scale height of around 11.5 km, which is a value typical of the Martian daytime. This relationship implies that dust is well-mixed within the vertical column.

2.3.1 Lifting mechanisms

Two main methods are postulated to explain the upwards transport of dust from the surface into the atmosphere. The first of these is near-surface wind stress, in which horizontal winds in the lowest atmospheric layer, if above a certain threshold value, can cause particles to be lifted from the surface into the main circulation. This threshold wind speed depends on such factors as dust particle size and density, and interparticle cohesion (stickiness). Direct lifting is supplemented by (or perhaps even outweighed by) saltation, whereby larger particles (generally of diameter $\geq$20 μm) may be partially lifted, falling short of entering into atmospheric suspension, but on returning to the surface collide with smaller particles, sending them into suspension [Sagan and Bagnold, 1975].

Transient convective vortices known as 'dust devils' provide the other main means for dust to enter the atmosphere. These structures, observed by Mars Pathfinder [Metzger et al., 1999] among others, can extend as high as the convective boundary layer (i.e. on the order 10 km) over a horizontal range of up to a hundred metres, and have low pressure centres which allow effective upwards advection of surface dust. Dust devils are most common, and strongest, at times of strong solar heating [Rennó et al., 2000].

2.3.2 Dust deposition

Dust particles will, over time, fall to the ground under the influence of gravity, as their density is greater than the atmospheric density. Settling velocity increases with particle size, with sedimentation timescales varying from days for large ($\sim$100 μm) particles to months for small particles (partly explaining the year-round baseline dust loading observed) [Read and Lewis, 2004].

However an important process in dust sedimentation is thought to be the 'scavenging' of dust particles by ice particles which form around them, with the dust particles acting as nucleation centres for cloud formation. The resulting dust/ice precipitate will fall faster than a typical dust particle, due to its greater size, reducing the dust settling time and effectively removing dust particles from the atmosphere. Due to this effect, the clearing of dust from the atmosphere may be a very non-linear process, since water condensation has a non-linear relationship to temperature, which itself is altered by dust levels [Clancy et al., 1996].

Scavenging is of particular importance in the polar regions in winter, when condensation of both water and carbon dioxide occurs. This leads to dust becoming cold-trapped along with water and CO_2 ice, affecting the albedo of the resulting 'dirty ice'. Paige and Ingersoll [1985] observed a higher albedo for the southern seasonal cap versus the northern cap, which may explain why the southern deposit persists year-round whereas the northern cap sublimes in summer. An important factor in causing these albedo differences could be increased amounts of dust deposited at the northern polar cap, due to the more extensive northern polar hood clouds leading to more dust particle scavenging [Clancy et al., 1996].

2.3.3 Martian dust storms

From the earliest observations of Mars it has been apparent that the obscuration due to dust varies greatly, both temporally and spatially. This is due to the formation of dust storms, both locally and globally. Small (local) storms cover 10^6 km^2 or less and last only a day or two, but larger storms can be formed from mergers between local events and can last for longer. Such storms can inject dust into the planet's main Hadley cell, intensifying the circulation via dust heating and enabling widespread dust transport, and potentially leading to a global storm [Lewis and Read, 2003]. The effect of such an event on IR dust opacity is shown in Figure 2.5.

The Viking landers experienced two global dust storms in 1977 [Clancy and Lee, 1991], but their occurrence is less regular than this may suggest. Planet-encircling storms are a less-than-annual event on Mars, and the reasons for they initiate in some years but not others are not fully understood, though may relate to the non-linear relationship with water condensation [Clancy et al., 1996], or changing surface dust coverage [Fenton et al., 2007]. They exclusively occur in southern spring/summer, and usually last for around 40–60° L_s, after which the reduced surface heating caused by the high dust opacity will cause a drop in near-surface wind strength and prevent further lifting. Local topography and the encountering of dust-free areas can also act to cause storm decay [Read and Lewis, 2004].

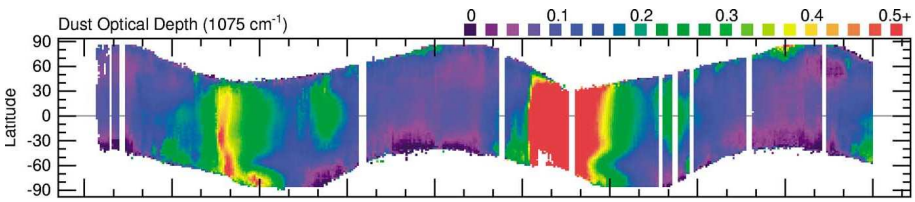

Figure 2.5: Dust optical depth (at 1075 cm^{-1}) over several Mars years (plot runs from $L_s = 90°$ in Mars Year (MY) 24 to $L_s = 180°$ in MY 26). A global dust storm occurred in the perihelion season of MY 25. From Smith [2004].

Chapter 3

Historic climates

3.1 Long term climate change

A theory summarised by Baker [2001] suggests how Mars could, on occasion throughout its history, have supported a warmer and wetter climate than it currently possesses. In this cyclic climate pattern, long cold and dry periods, such as we observe at present, are interspersed with transient periods in which water can exist in liquid form, as precipitation and even an ocean. The trigger for these climate changes is proposed to be huge volcanic episodes, which expel carbon dioxide and other material into the atmosphere causing a greenhouse warming effect, allowing ground ice to melt, and allowing additional water to upwell from beneath the surface. Over time, however, CO_2 is lost back into the subsurface, and the standing water evaporates and is transported as vapour to the poles, where it precipitates and accumulates as ice deposits. The pressure and temperature drop, and the climate returns to its original state.

In present Martian conditions, the occurrence of water in the liquid phase is a probably a rare event [Haberle et al., 2001] (although there is some recent evidence for the observation of liquid water in the form of a brine [Renno et al., 2008]), as over much of the planet surface pressure is below that of the triple point of water. At these pressures, water moves between the solid and vapour phases only, depending on temperature. However, several ancient planetary features point to the existence of liquid water in some past climate regime. The southern highlands contain networks of tributaries several kilometres wide which provide strong evidence for previous persistent water flow, and there is evidence in impact basins for the existence of lakes.

Huge outflow channels (some tens of kilometres wide) are present to the east of the Tharsis region and indicate large-scale flooding of the northern lowlands. The possibility of an ocean once covering most of the northern hemisphere has been considered [Parker et al., 1993], with Head et al. [1999] suggesting that such an ocean might have contained 10^7 km^3 of water, reaching an average depth of 560 m. Explanations for the disappearance of this large amount of

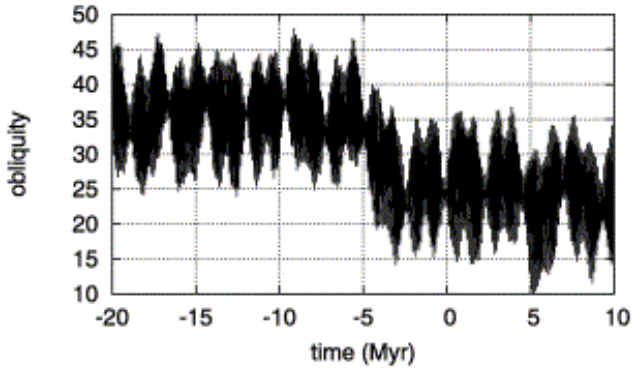

Figure 3.1: From Laskar et al. [2004], showing the predicted change in orbital obliquity (in degrees) for the recent past and future.

water include loss to space, condensation onto the polar caps, or absorption into the subsurface groundwater system.

The total capacity of the megaregolith has been estimated to be as much as 2 x 10^8 km^3, equivalent to a global water depth of 1400 m, depending on the mean porosity of the subsurface [Clifford, 1993].

3.2 Orbital timescale variation

More recently (on timescales of 10^4–10^5 yr) climate change on Mars has been driven by variations in its orbital cycle, as described by three main parameters: the orbital obliquity, (the angle that the rotation pole makes with the normal to the orbital plane), the eccentricity of the orbit, and the solar longitude at perihelion. Mars is currently at an obliquity of around 25°, similar to that of Earth, but this varies with a much greater amplitude than it does for Earth. Statistical predictions of the history of this chaotic orbit allow a range of 0°–60° over the past 250 Myr [Laskar and Robutel, 1993]. During the last 5 Myr, Mars' obliquity has oscillated within the range 15°–35°, but prior to this (5–20 Myr ago) its mean value modulated to ∼35°, with a similar ±10° variation allowing obliquity to reach ∼45° [Laskar et al., 2004].

Eccentricity has oscillated in the range 0–0.12 over the last 25 Myr (currently ∼0.093), possibly extending to 0.16 or so earlier in the planet's life, though the mean eccentricity on the Gyr timescale is smaller than present, at ∼0.069 [Laskar et al., 2004]. Perihelion (the closest approach to the Sun) currently occurs at $L_s = 251°$, in southern summer, but the orbit precesses with a period of ∼50 kyr, so that the timing of perihelion reverses between southern and northern summer every 25,000 years [Ward, 1974].

3.2.1 Effect of obliquity change

Changes in obliquity affect the distribution of solar heating between equatorial and polar regions. At low obliquity (<20°) a large portion of the CO_2 atmosphere condenses permanently onto the polar caps, lowering the global atmospheric pressure by a factor of two or more [Fanale and Salvail, 1994]. Higher obliquities, at which polar heating is increased, do not allow perennial CO_2 caps to form, though atmospheric pressure remains on average fairly similar to the current value, as additional carbon dioxide adsorbed in the regolith tends not to be released to the atmosphere despite the higher average temperatures [Fanale and Salvail, 1994].

A low-obliquity drop in atmospheric pressure should cause a dramatic reduction in dust loading, as the threshold wind speed for lifting increases while the wind speed distribution is relatively unaltered [Pollack and Toon, 1982]. Conversely, at high obliquity lifting becomes easier and dust levels increase greatly, helped by the positive feedback set up as dust causes atmospheric heating and strengthens the circulation. Thus global dust storms become much more common, perhaps even occurring over much of the year, and optical depths increase. GCM studies from Newman et al. [2005] and Haberle et al. [2003] confirmed these hypotheses; Newman et al. [2005] also found evidence for deposition in polar regions increasing in periods of high obliquity.

Another important change due to variations in obliquity concerns the stability of surface and near-subsurface water ice. Higher obliquity allows more vapour to be released annually into the atmosphere, with the higher humidity causing the region of surface ice stability (currently limited to polar regions) to extend equatorward, and also allowing non-polar subsurface ice to form closer to the surface. When obliquity then decreases, the ice stability zone shrinks back to the pole, with ice subliming from the mid-latitudes. The dessication of this 30°–60° 'mantle', observed in both hemispheres [Mustard et al., 2001], leaves behind surface lag deposits which may insulate against further sublimation from the regolith [Head et al., 2003].

This cycling between high (>30°) and lower obliquity denotes the shifting of the Martian climate between glacial (ice-age) and interglacial periods. Martian 'ice ages' are periods in which ice and dust are transported to the mid-latitudes, and contrary to Earth, glacial periods on Mars actually see an increase in average polar temperatures. Over the last ∼300 kyr, obliquity has stayed close to its current value, so this period is referred to as interglacial, and has seen a removal of ice from the mid-latitude mantle and transport toward the poles.

3.2.2 Emplacement of the polar layered deposits

The PLD act as a record of past climate regimes, in the sense that they provide information on water ice deposition rates and dust content of the polar regions. The prevailing theory of their formation is that it results from quasi-periodic climate change brought on by variations in obliquity, eccentricity and argument of perihelion [Cutts and Lewis, 1982]. In particular, the dust/water ice ratio

of polar deposits should increase with obliquity due to the increase in occurrence of global dust storms. PLD structure may also depend on more complex mechanisms though, including local climate effects, aeolian processes, and 'lag' deposits (dust left behind as ice sublimes off due to a change in conditions) [Milkovich and Head, 2005].

As mentioned in the previous chapter (2.2.2), the Clancy effect (which drives water towards the hemisphere for which winter occurs at perihelion) predicts that the wettest hemisphere should alternate as the timing of perihelion changes between southern and northern summertime. Therefore, if indeed the northern water ice cap is growing at the expense of the southern cap in present conditions, this situation could have been reversed ∼25,000 years ago. As the orbit precesses then, repeated growth and decay of both residual ice caps is predicted, allowing for layering to exist at both poles, depending on the relative deposition and sublimation rates in successive climatic periods.

Clancy et al. [1996] estimated that for full cycling of the caps between the poles within the timescale dictated by the orbital precession, the ice caps would need to sublime at a rate two orders of magnitude faster than the $\leq$1 mm yr^{-1} current sublimation rate found by Haberle and Jakosky [1990]. This is most plausible during periods of higher obliquity, when polar insolation levels are increased.

Furthermore, at times of low eccentricity, seasonal hemispheric differences are reduced, suggesting little pole-to-pole water transfer, though some bias may still exist due to the topographic dichotomy [Richardson and Wilson, 2002, Montmessin et al., 2007]. It is likely that the complex interplay between the obliquity, eccentricity and perihelion precession cycles determines specific periods in which removal and deposition of water ice can occur.

The lack of impact craters in the north polar region places an upper limit on the age of the northern layered terrains, at around 10-100 kyr [Montmessin, 2006]. The southern polar terrain, on the other hand, shows impacts dating back several million years, longer than the timescale of obliquity variation Plaut et al. [1988]. The more active resurfacing seemingly taking place at the north pole could be caused by a greater net (i.e. over the full perihelion precession cycle) ice and dust accumulation there, as allowed by the south-north topographic asymmetry [Richardson and Wilson, 2002].

Chapter 4

The UK Mars GCM

In the absence of extensive observational data for Mars, General Circulation Models (GCMs) have emerged as the primary tool with which to analyse many aspects of the Martian climate system. There exist a handful of these models around the world today, and inter-comparison between models, as well as direct reference to (or assimilation with) real data, provides stringent tests of their reliability.

4.1 General Circulation Models for Mars

The first Mars GCMs were adapted from similar models used for Earth, dating as far back as 1969 with the model of Leovy and Mintz [1969], which now exists in the form of the NASA Ames GCM, based in California [Haberle et al., 1993]. Other GCMs currently in use include models at the Geophysical Fluid Dynamics Laboratory (GFDL) in Princeton, and at the Laboratoire de Météorologie Dynamique (LMD) in France, with the latter originating in the late eighties, not long before the UK Mars GCM (UKMGCM), which is now shared between Oxford University and the Open University, based in Milton Keynes.

Shortly after the European models' conception, the LMD and Oxford groups began to work closely together in developing additional physics schemes for the two models. The package of physics modules is now largely shared by the LMD and UK MGCMs, but the dynamical cores of the two remain distinct. The LMD model uses the finite-difference method for solving the hydrodynamical equations, by discretisation onto a longitude-latitude grid. The UKMGCM on the other hand utilises a spectral dynamical solver, in which horizontal fields are represented by a truncated (at a point defined by the resolution being used) series of spherical harmonic basis functions. The differing model cores provide a useful means of comparison to identify any weaknesses inherent in either numerical method [Forget et al., 1999].

4.2 Model dynamics

The dynamics of the UKMGCM involve solution of the hydrostatic primitive equations, discretised spectrally as mentioned above, based on the method of Hoskins and Simmons [1975]. Three of the equations come from the components of the Navier-Stokes equation, with some simplifications, neglecting some smaller magnitude terms:

$$\frac{Du}{Dt} - \left(2\Omega \sin\phi + \frac{u \tan\phi}{a}\right) v + \frac{1}{\rho a \cos\phi} \frac{\partial p}{\partial \lambda} = F_\lambda \tag{4.1}$$

$$\frac{Dv}{Dt} + \left(2\Omega \sin\phi + \frac{u \tan\phi}{a}\right) u + \frac{1}{\rho} \frac{\partial p}{\partial \phi} = F_\phi \tag{4.2}$$

$$g + \frac{1}{\rho} \frac{\partial p}{\partial z} = 0 \tag{4.3}$$

Here spherical coordinates λ, ϕ and z denote longitude, latitude and height respectively, a is the planetary radius, Ω is the angular rotation rate, $F_{\lambda,\phi}$ are horizontal frictional force components, and velocities (eastward, northward and upward) are given by

$$(u, v, w) \equiv \left(a \cos\phi \frac{D\lambda}{Dt}, a \frac{D\phi}{Dt}, \frac{Dz}{Dt}\right)$$

where the advective derivative in spherical coordinates is

$$\frac{D}{Dt} \equiv \frac{\partial}{\partial t} + \frac{u}{a \cos\phi} \frac{\partial}{\partial \lambda} + \frac{v}{a} \frac{\partial}{\partial \phi} + w \frac{\partial}{\partial z}$$

Vertically, the hydrostatic approximation is used. Additionally, the continuity equation

$$\frac{D\rho}{Dt} + \rho \nabla \cdot \boldsymbol{u} = 0 \tag{4.4}$$

where $\boldsymbol{u} = (u, v, w)$; the ideal gas equation

$$p = R\rho T; \tag{4.5}$$

and a thermodynamic energy equation

$$\frac{D\theta}{Dt} = Q \tag{4.6}$$

where θ is potential temperature and Q represents diabatic heating, are used.

The model uses the terrain-following sigma system as the vertical co-ordinate (in finite difference form, with typically twenty-five levels, spaced more closely together near the surface), where sigma is defined as the pressure at a particular height divided by the corresponding surface pressure. Model height then varies with surface elevation (currently based on Mars Orbiter Laser Altimeter data) and atmospheric conditions, but typically extends to around 100 km. In the upper levels a sponge layer is used to reduce unphysical reflections of vertically propagating waves from the top boundary [Forget et al., 1999].

4.3 Physical processes in the UKMGCM

4.3.1 Radiative transfer

Atmospheric absorption and emission is considered by the UKMGCM to be dependent only on the presence of carbon dioxide and dust, though it is expected that water ice clouds will be added to this list in future. The CO_2 radiative code uses an improved version of the wideband 15-μm scheme from Hourdin [1992]. Non-local thermodynamic equilibrium effects and shortwave, near-infrared CO_2 absorption of incoming solar radiation become significant at higher altitudes, and are calculated by the model [Forget et al., 1999].

The effect of solar radiation on atmospheric dust is calculated following methods used in terrestrial GCMs, with upward and downward fluxes at each level found using the Delta-Eddington approximation. Two widebands in the near-IR are used. Scattering by dust of thermal infrared radiation applies outside the 15 μm band, and is computed using properties chosen to match the Mariner 9 observations of the 1971 dust storm [Forget et al., 1999]. The ratio of visible to infrared opacity, $\tau_{0.67\mu m}/\tau_{9\mu m}$, one of several poorly constrained parameters in the dust radiation scheme, is set to 2, following Forget [1998].

4.3.2 The CO_2 cycle

Unlike terrestrial GCMs, models of Mars must include the periodic condensation and sublimation of a significant portion of the CO_2 atmosphere. Condensation occurs whenever a gridpoint falls below the CO_2 condensation temperature ($\sim$140 K at Martian pressures), and latent heat is released to keep the gridbox at the condensation point. Sublimation occurs to keep the CO_2 at the frost point. CO_2 snowfall is simulated, with descending solid particles allowed to resublime if they reach a sufficiently warmer lower gridbox. Surface albedo is increased where there is CO_2 ice cover, and emissivity is decreased during condensation to simulate freshly deposited snow and ice cloud effects [Forget et al., 1999]. In the future it may become possible to model CO_2 regolith adsorption and/or cloud formation, in a similar manner to that used for water (4.4.2).

4.3.3 Surface processes

Surface temperature is determined not only by incoming and outgoing radiation fluxes but also by thermal conduction in the soil beneath. The UKMGCM includes an 11-layer soil diffusion scheme, extending down to depths defined by the thermal inertia of the surface gridpoint, so as to accommodate the penetration of the thermal wave on diurnal and annual timescales [Read and Lewis, 2004].

4.3.4 Sub-gridscale effects

Since the horizontal resolution of GCMs is on the order of 100 km, only large-scale atmospheric motion is simulated directly, and localised phenomena, which

can affect the general circulation, must be parameterised. Turbulence and convective mixing within the boundary layer are handled using a turbulent closure scheme, allowing winds, potential temperature and tracers to be moved realistically through the boundary layer. Gravity wave generation and topographic drag on the low-level flow, due to fine-scale topography within a surface gridbox, are also parameterised [Collins et al., 1997, Forget et al., 1999].

4.4 Tracer transport and physics

An atmospheric tracer is any component that moves following the general circulation pattern, possibly acting to influence the circulation (active) or simply following the mean flow (passive). The UKMGCM contains a tracer transport scheme, and the associated physics necessary to model either dust lifting and transport, or the water cycle. Both airborne dust and water vapour are advected using a semi-Lagrangian numerical method, including Priestley's method of mass conservation [Priestley, 1993].

However, as an artefact of the concurrent addition of the two schemes, the model is not set up to simulate both cycles at the same time. Thus, the two options for running with tracer transport (at present) are either to use the dust lifting, transport and sedimentation schemes, without considering water, or to model water vapour transport and ice formation, using a 'prescribed' dust distribution to, as realistically as possible, represent the atmospheric opacity that arises due to suspended dust.

In the second case, prescribed dust is assumed to be vertically well-mixed up to a certain height, with fairly constant mixing ratios, which then fall away at higher altitudes. Functionally this situation is modelled by

$$q = q_0 \exp\{0.007[1 - (p_0/p)^{70km/z_{max}}]\} \tag{4.7}$$

where q is dust mixing ratio at a given height with pressure p, q_0 and p_0 are the surface mixing ratio and surface pressure, and z_{max} represents the top of the dust layer (modelled with variation in latitude and time, and defined as the height at which dust concentration has fallen to one thousandth of its surface value) [Read and Lewis, 2004]. q_0 (again a function of latitude and time) is then chosen to give the desired optical depth at the surface, with the 'MGS' scenario, modelled on TES observations and giving a simplified reproduction of a 'typical' (i.e. without global dust storm) Martian year, a commonly used form.

4.4.1 Dust

Dust lifting and transport were added to the UKMGCM by Newman et al. [2002], using (as described above) a semi-Lagrangian material advection scheme, and two forms of parameterised lifting, namely by near-surface wind stress, and by dust devils. These processes have been described previously (2.3.1). Dust can be chosen as either passive or active — in the passive case, the radiation

code continues to refer to the prescribed opacity function mentioned above, regardless of dust movement, but in the active mode, atmospheric opacity is calculated at each timestep from the transported dust field.

The drag velocity u_{drag} at the surface (responsible for wind stress lifting) is taken from the velocity in the lowest atmospheric level $u(z_1)$ according to

$$u_{drag} = \frac{ku(z_1)}{\ln\left(\frac{z_1}{z_0}\right)} \tag{4.8}$$

where k is von Karman's constant ($= 0.4$), z_1 is height of the lowest model level ($\sim$5 m) and z_0 is the roughness height, $= 0.01$ m. For lifting to occur, this must be greater than a threshold wind velocity u^t_{drag}, derived semi-empirically. The importance of saltation in lifting particles of the size observed to be in the atmosphere is accounted for by setting the actual vertical particle flux proportional to the saltating sand particle flux (in a form due to White [1979] that depends on u_{drag} and u^t_{drag}), with a proportionality constant (the 'lifting efficiency') whose value is tuned to provide realistic lifting rates. In addition, a 'gustiness parameter' is defined to capture the increased lifting effect of small-scale wind speed variations about the mean (i.e. large-scale) value produced by the model.

The flux due to dust devil lifting is calculated in a similar way, as being proportional to the 'dust devil activity' Λ, defined to be equal to the product of the thermodynamic efficiency of the dust devil convective heat engine (dependent on pressures at the top and bottom of the boundary layer) and the sensible heat flux at the base of the vortex.

Once lifted into the lowest model layer by either method, the dust is rapidly mixed up through the boundary layer by the turbulent diffusion scheme. It is advected horizontally by the transport scheme, and falls vertically down through model levels under the influence of gravity, eventually reaching the surface. The surface is assumed to have an infinite supply of dust, except at the polar caps, where no lifting takes place.

4.4.2 Water

The water cycle code, implemented by Böttger et al. [2005] consists of vapour advection using the same semi-Lagrangian scheme mentioned above, a simple bulk cloud scheme, ice sedimentation and surface deposition, and subsurface diffusion using a method adapted from the 1-D model of Zent et al. [1993].

Water is supplied to the atmosphere through sublimation of surface ice, at a rate determined by the flux equation

$$F = \rho C_d |u| (q_{atm} - q_{sat}) \tag{4.9}$$

where ρ is the atmospheric density in the lowest model level, C_d is the drag coefficient, u is the wind velocity in the lowest level, q_{atm} is the mass mixing ratio of vapour in the lowest level, and q_{sat} is the saturation vapour mixing ratio at the temperature of the surface. Vapour is then vertically diffused up through the boundary layer, and transported by the advection scheme.

If the vapour pressure of a particular gridbox is greater than the saturation vapour pressure, excess vapour forms ice clouds to return the gridbox to saturation. These ice particles, with radius set to 2 μm to match observations, then sediment in the same way as dust, but have the potential to resublime if they reach a lower altitude gridbox that is below saturation; otherwise ground ice forms on the surface.

The 11-layer regolith model extends to depths of a few metres (varying spatially depending on the thermal inertia at the surface) and allows subsurface water to exist as vapour, ice or adsorbate. Adsorption of water onto regolith grains is modelled using the relationship

$$\alpha = \rho_s \frac{\beta P^{0.51}}{e^{\frac{\delta}{T}}} \tag{4.10}$$

where α is the density of adsorbate, ρ_s is the regolith density, P is the partial vapour pressure, T is the soil temperature (found from the scheme described in 4.3.3), and β and δ are constants. Partition between the three forms is determined by an implicit scheme, with the adsorbed and vapour phases related through $P = \frac{nkT}{m_w}$, and ice forming above saturation as in the cloud scheme.

Water moves vertically between the regolith levels according to the diffusion equation

$$\frac{\partial n}{\partial t} = D \frac{\partial^2 n}{\partial z^2} \tag{4.11}$$

where n is the vapour density and D is the diffusion coefficient. Zero flux is imposed at the bottom boundary.

The major weakness of the water scheme, currently, is the lack of radiatively active clouds. This becomes especially apparent in climates wetter than the present one (see 6.2). Also of great importance is the addition of a microphysical cloud scheme, to allow multiple cloud particle sizes and to take into account the possibility of cloud formation in sub-saturated gridboxes, by means of heterogeneous nucleation, dependent on the presence of dust aerosol particles. It is anticipated that part of the UKMGCM physics scheme will be updated in the near future, through collaboration with the LMD team — this would address some of the issues raised here, with further improvement being one of the goals of my project.

Refinements could also be made to the regolith scheme, including the use of a more accurate function for calculating regolith adsorption (to replace Equation 4.10), allowing regolith thermal inertia to change in the presence of ice, altering the operation of subsurface exchange to take into account the potentially blocking effect of thick overlying ground ice, and perhaps some preferential direct surface condensation (see 5.2.1).

Chapter 5

Model construction and preparation for past-climate simulations

5.1 Setting up a working model code

In the years following the development of the two tracer schemes described in 4.4, the UKMGCM has been ported from running on DEC Unix ('alpha') to the now-more-common Linux system. Due to subtle differences in the operation of the two systems, transferring the code across was not a trivial matter — rigorous checking of the new output was carried out in recent years, but with a focus only on the non-transporting version of the UKMGCM. Thus, as of last year, the transport scheme as well as the dust and water physics modules were yet to be tested on the new Linux operating system.

Since a working version of the water-transporting UKMGCM was no longer available even on the older alpha computers, it was decided that I would add the relevant components of the original water scheme to the existing (i.e. validated for Linux) non-transporting MGCM code, to create a water-transporting code capable of operating on the faster Linux computers. This would enable the running of several past-climate simulations (described below) in the short term, and serve as a preliminary exercise for the creation of a generalised transport code for Linux, a task which is currently underway.

Getting the code working satisfactorily on Linux took some time, with conservation of mass within the tracer transport module proving particularly problematic. However, a working version of the water-transporting code was successfully formulated, and used for the experiments described below. Tracer mass conservation could still be improved — a proposed increase in precision across the MGCM physics modules may achieve this.

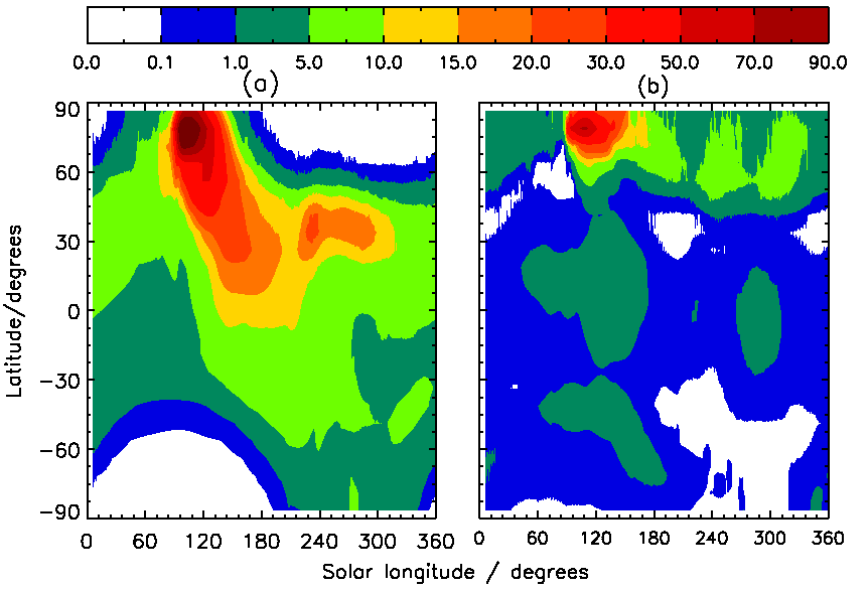

Figure 5.1: Model cycle for zonal mean vapour (a) and clouds (b), in prμm, using a large cap source and initially empty regolith.

5.2 Reproduction of the present water cycle

A typical water-transporting MGCM run uses a north polar water ice cap source, which sublimes in summer, supplying the atmosphere with water. For the horizontal grid resolution used throughout this work (that is, gridboxes 7.5° by 7.5° in size), properly representing the shape of the residual water ice cap is not possible. One approximation, which overestimates the cap size, sets an effectively infinite amount of surface ice at each gridpoint within the two most northerly latitude bands (extending from the pole to 75°N). A more accurate approach places ice around the most northerly band, and at selected longitudes on the next latitude band. The model can be started with the regolith either dry or containing some prescribed distribution of water and ice.

The UKMGCM is capable of producing an annual water cycle that is in reasonable agreement with observations (e.g. Figure 2.1). Output from the third year of a simulation using an initially dry regolith and a large north polar cap is shown in Figure 5.1 (a). The general form of the annual cycle is clearly present, though most noticeably the northern summer maximum, at more than 100 prμm, is overestimated. This is a result of the model cap source being too large — however, when a 'real' cap source is used instead, the peak is reduced to around 30 prμm, a value significantly lower than the observed maximum. Moreover, after running for two or more years (the atmosphere tends to lose water to the subsurface once the 'dry' regolith is turned on), both source sizes

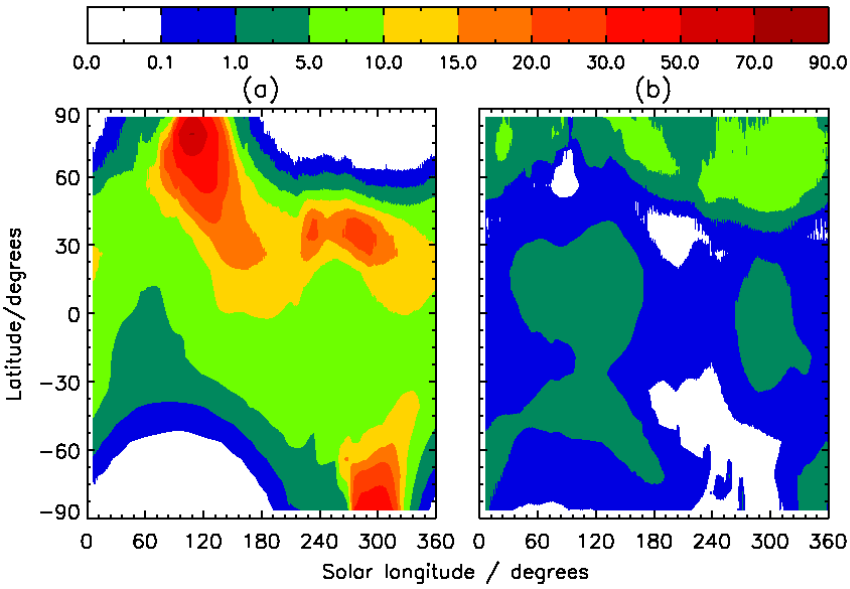

Figure 5.2: Same output as Figure 5.1, but with a more realistic north polar cap size, and regolith initialised with similar amounts of water at each pole (showing the second year after the regolith was turned on).

result in a southern summer maximum that is too low, at less than 10 prμm, compared to the observed value of $\sim$30 prμm.

It has been suggested that regolith desorption contributes to the northern summer peak, and indeed the model water cycle does vary strongly with initial regolith distribution. Including water in the polar regolith, following Mars Odyssey observations, does boost the observed vapour maxima, and subsurface amounts can to some extent be varied to give a desired atmospheric vapour level (Figure 5.2 (a)). At present, regolith ice densities much less than the $\sim$50% mass fractions estimated to exist in the polar subsurface must be used to give a reasonable atmospheric vapour cycle. This is probably because, in reality, regolith desorption (and adsorption) is locally blocked by the seasonal and residual caps, so it may be that changing the operation of the regolith (as suggested in 4.4.2) will improve water cycle reproduction, by shutting off atmosphere-subsurface exchange when surface ice is present.

Polar hood and aphelion belt clouds are also reproduced (Figure 5.1 (b)) by the model. The large amount of cloud ice seen over the northern summer pole are due to the unrealistic amount of vapour subliming off a large polar cap; this peak in cloud amount is greatly lessened with a more realistic cap size (Figure 5.2 (b)). Inaccuracies probably also arise due to the simplistic cloud scheme, and the model overestimates cloud abundances in comparison with observations.

5.2.1 Improved surface condensation

An issue requiring further attention is that of striking a balance between adsorption of atmospheric vapour by the regolith, and direct condensation of vapour onto the surface below (provided its temperature is below the temperature of saturation for the vapour pressure in the lowest atmospheric level). This surface condensation (from the lowest model layer) is modelled by the UKMGCM only when the regolith scheme is not being used; otherwise the surface is assumed to be completely porous, and any downward vapour flux (as determined by Equation 4.9) enters directly into the regolith. In reality a certain amount of freezing out on the surface seems likely, but this has not yet been modelled.

In the short-term, however, a more minor improvement to the scheme was possible, by allowing condensation onto the surface whenever subsurface ice is present in the upper-most soil level, as regolith-atmosphere exchange is already disabled in this case — the regolith is said to be 'ice-choked', with any diffusion into or out of it blocked. The difference due to this change is slight in present conditions, as subsurface ice forms mainly at the north pole, so the main effect is that some north polar vapour recondenses onto the seasonal cap.

5.3 Orbital-change simulations

General circulation models offer a method with which to investigate how past Martian climates may have differed from that observed today. Relatively recent climate variations, such as those brought on by changes in the planet's orbital parameters (as described in 3.2), are most suitable for study with current GCMs due to the lack of significant changes in terrain or atmospheric make-up expected over such timescales.

Several such studies have been done in recent years, either looking at changes in dust lifting patterns [Haberle et al., 2003, Newman et al., 2005], or various aspects of the water cycle — Mischna et al. [2003] carried out several increased-obliquity experiments to investigate regions of surface ice formation, and Forget et al. [2006] examined more localised glacier formation at high obliquity.

No studies have yet been conducted with simultaneous modelling of the dust and water cycles — prescribed dust distributions have been used for any water-transporting experiments. For the two examples mentioned already, the opacity function was merely that which matches current observations, though Montmessin et al. [2007] and very recently Madeleine et al. [2009] have attempted to more accurately represent a typical dust loading for the climate scenario under investigation, as is the aim here. Opacity functions used here are more detailed than previous efforts, as neither Montmessin et al. [2007] nor Madeleine et al. [2009] included any meridional variation in opacity, preferring a simple scaling across the planet. It is hoped that this more precise representation of dust opacity leads to a better reproduction of past climate systems.

5.3.1 Dust distributions for past climate scenarios

To attempt to represent the dust loadings expected under orbital conditions different to those experienced on Mars today, data from a previous variable-obliquity study by Newman et al. [2005] were used to derive dust opacity functions appropriate to the orbital regimes studied. In accordance with the data available, obliquities of 15°, 25° (i.e. present-day) and 35° were considered, along with a 'reversed-perihelion' case, in which obliquity is kept at 25° but the timing of perihelion is shifted by 180° to $L_s = 71°$, during northern summer.

The simulations of Newman et al. [2005] had the aim of studying changes in dust lifting patterns, and used lifting parameters chosen (for radiatively inactive atmospheric dust; see 4.4.1) to replicate observed dust optical depths for current conditions. The two lifting mechanisms, near surface wind stress lifting and dust devil lifting (see 2.3.1), were tuned separately, such that the combined dust lifted into the atmosphere actually gives optical depths that are too high by about a factor of two. However, due to the changing relative importance of each lifting method with varying obliquity, both should be considered in order to accurately simulate lifting rates upon change of orbital parameters.

For 25° obliquity, simply taking the average of the optical depths produced by each of the two lifting mechanisms gives a realistic form of the annual opacity cycle, with visible opacities at low latitudes of ∼0.2 over much of the year, and a peak of around 1 near perihelion, which is somewhere in between the peak opacities expected during years with and without a global dust storm. Since no tuning of dust loadings to match observations is possible for conditions different to the present, this approach was extended to the other orbital regimes being considered.

The dust-transporting simulations of Newman et al. [2005] did not take into account the positive feedback that applies for radiatively active wind stress lifting (as increased dust loading strengthens the mean circulation, increasing surface wind velocity and allowing further lifting), therefore the contribution to opacity of this lifting type is probably underestimated. Conversely, dust devil lifting responds to increases in atmospheric dust loading via a negative feedback (due to reduction in near-surface vertical temperature gradients), so dust devil lifting rates may be overestimated at certain (dustier) times of year. Further uncertainty in the optical depth distributions arises due to the unknown (and unmodelled) effect of a finite supply of surface dust, which may act to limit the peak opacity at high obliquities.

In each case, visible opacity due to atmospheric dust was calculated, referenced to a 610 Pa height level to remove the effect of topography. Longitudinal opacity variations were seen to be small, so zonal uniformity was assumed for simplicity (as it is in the case of the 'MGS' dust scenario used routinely by the UKMGCM). Analytic representations of the opacity distributions were then formed as functions of latitude and solar longitude, and are shown in Figure 5.3. The standard opacity distribution used for present day simulations is shown in Figure 5.4 for comparison with Figure 5.3 (a).

The opacity function for present day conditions compares well with the MGS

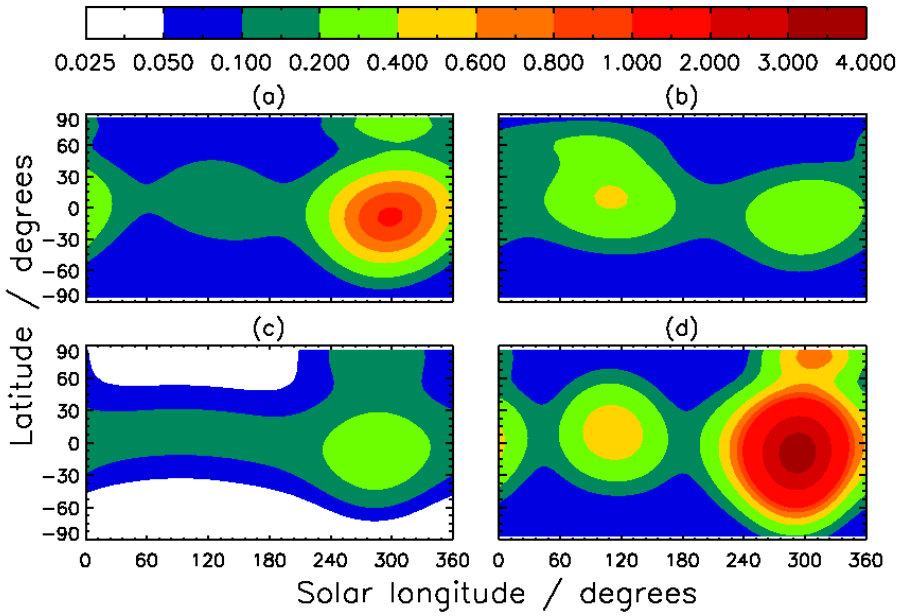

Figure 5.3: Dust visible opacity (at 610 Pa) for (a) 25° obliquity; (b) Reversed perihelion (25°); (c) 15° obliquity; (d) 35° obliquity.

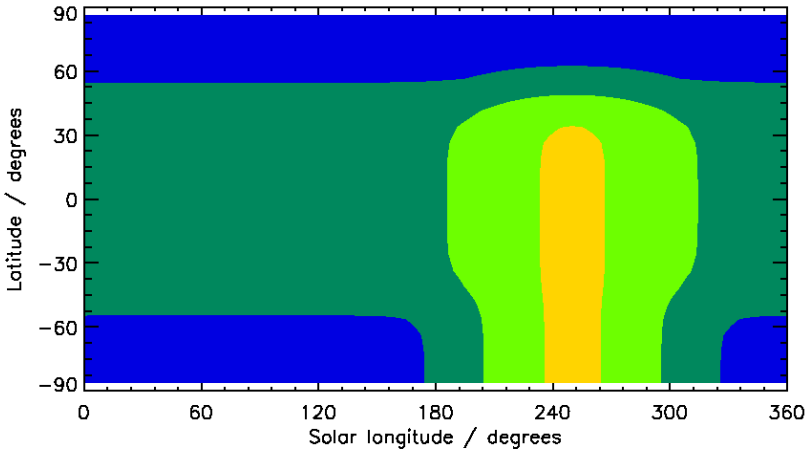

Figure 5.4: Dust visible opacity (at 610 Pa) for present conditions, according to the 'MGS' scenario. Contour levels are the same as in Figure 5.3.

scenario (as it should do) through northern spring and summer, with opacity reaching higher values than MGS near perihelion. This is not unreasonable, as the MGS distribution applies to a southern summer season in which no global dust storm occurs, and thus is only representative of some Mars years.

The 35° obliquity opacity rises higher still in southern summer, due to a strong global dust storm and large amounts of near surface wind stress lifting. Conversely, an obliquity of 15° sees lower optical depths, with the annual pattern remaining qualitatively similar to that at 25° and 35°, and dust devil lifting becoming the dominant process. The reversed perihelion case shows a much more uniform optical depth, without a northern summer (perihelion) peak comparable to the southern summer maximum seen at present. That the opacity distribution is not merely a mirror image of the present-day distribution can be attributed to mean circulation (and thus lifting) biases arising from the hemispheric dichotomy [Newman et al., 2005].

5.3.2 Simulations carried out

Runs using an initially dry regolith were performed for each of the scenarios mentioned previously (15°, 25° and 35° obliquity, and the reversed perihelion case at 25°), under the MGS dust scenario, with the first (spin-up) year of each having the regolith turned off, to allow water to be more efficiently transported from the north polar source over the whole planet. From the second year onwards, the regolith scheme was switched on, and each simulation was computed over four more years. Similar runs were then carried out using the dust distributions described above, starting from the end of the spin-up year done with MGS dust. An overly large north polar cap (as explained in 5.2) was used, meaning northern summer vapour maxima are overestimated.

Also, using the derived dust distributions, the 35° and reversed perihelion scenarios were rerun with the regolith initialised with a subsurface water/ice distribution of the form observed by Mars Odyssey; that is, ice at both poles, with the southern deposits overlain by several dry soil levels. The more realistic cap size was used for these runs, and the changes in output over the previous simulations were examined. The 15° case, as is explained in 6.4, in fact requires a regolith water source to hydrate the atmosphere.

For the experiments, it was necessary to alter the code to have the surface albedo change appropriately in the presence of surface water ice, away from the north pole (where albedo due to the residual ice cap is already correct). This was to allow for the possibility of surface ice existing separately from the seasonal CO_2 caps — under present-day conditions this does not occur (apart from the north residual cap) so model surface albedo simply follows CO_2 ice.

The specific water ice albedo value would, in reality, depend on the thickness of the ice deposit, as well as the amount of dust trapped within the sedimenting cloud particles. This latter consideration is something which will hopefully be modelled by the UKMGCM in future, but for now, albedo is set to 0.4 whenever 5 μm or more of water ice are present in a surface gridbox (following Montmessin et al. [2007] and others).

Chapter 6

Initial past climate study results

6.1 Changes in surface pressure

Shown in Figure 6.1 are the annual pressure cycles for each scenario being studied, using the MGS dust distribution. At 25°, average surface pressure oscillates about a mean of around 600 Pa, with a minimum at $L_s = 150°$ (aphelion) when global insolation is at its lowest, causing a significant fraction of the atmosphere to condense onto the southern polar cap. A secondary minimum occurs during northern winter, due to the shorter and warmer nature of this season, compared to southern winter. The cycle at 35° follows a similar form, with a deeper aphelion (perihelion) minimum due to the south (north) pole being tilted further away from the Sun at this time, and thus cooling more dramatically.

The 15° obliquity simulation was spun up over a period of around thirty Martian years (by Newman et al. [2005]), to allow the pressure cycle to equilibrate — a large portion of the CO_2 atmosphere gradually condenses out, forming permanent caps at both poles (where insolation levels are low) and bringing global surface pressure down to an average of less than 400 Pa. Some oscillation in cap size still occurs, but with a lower amplitude than at 25°. The model of Fanale and Salvail [1994] suggests that such an equilibration is not necessary for higher obliquity, when no permanent polar caps exist, due to a balance between regolith adsorption and desorption of carbon dioxide leading to little variation in average pressure.

The reversed perihelion case shows the deeper minimum now to be due to the formation of the northern cap, which now occurs during aphelion season. However, the cycle is not a simple mirror-image of the present-day cycle — the main minimum has a greater amplitude than at 25°, indicating that the northern cap grows larger than the southern cap does at the current orbital parameters. Similarly, the secondary minimum is less significant for reversed perihelion, due to a slightly smaller perihelion cap forming (at the south pole). The reasons

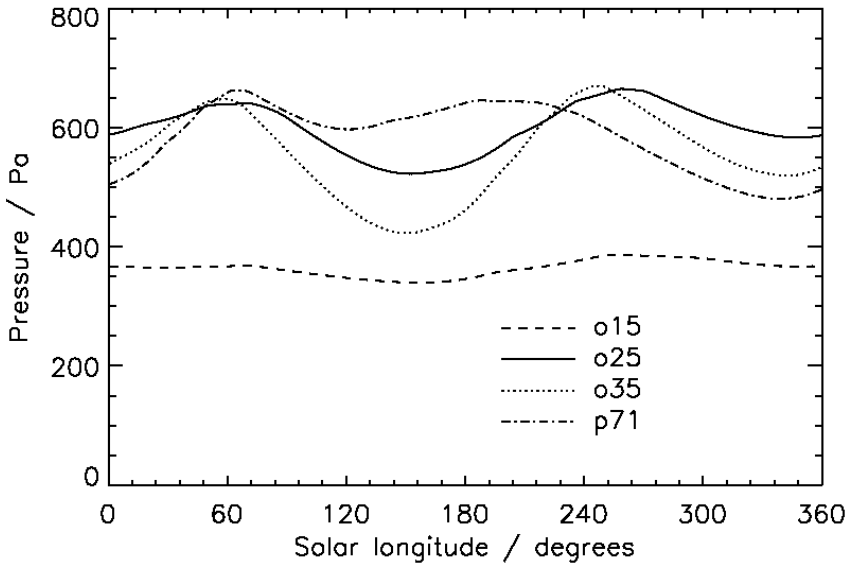

Figure 6.1: Annual pressure cycles for each set of orbital parameters being studied.

for this lack of symmetry are dynamical, most likely due to the hemispheric difference in topography ([Richardson and Wilson, 2002]) favouring a northward carbon dioxide condensation flow, rather than deposition at the south pole.

6.2 Increased obliquity

The vapour cycle at an obliquity of 35° is qualitatively very similar to the pattern observed currently, but with an approximate one order of magnitude increase in humidity across the planet. Results for both of the optical depth distributions used are shown in Figure 6.2. The north polar maximum is in excess of 700 prμm, with the southern maximum a little less than this. The southern peak is larger when the 35° opacity function is used, due to the decrease in optical depth (and therefore increase in surface heating) over the southern summer pole, and exhibits a double-peaked structure in this case, with distinct maxima at L_s = 250° and L_s = 275–300°. The first of these corresponds to the removal of the seasonal ice cap, and the second vapour peak is formed by water released from the regolith, at the point of peak surface temperature (>275 K).

Using a more realistic north polar cap size and a regolith initialised with amounts of polar water and ice, as expected, brings the two peaks closer together in magnitude. 300–400 prμm of vapour are observed at each summer pole, with the southern maximum retaining its double-peaked form.

With a present-day dust loading, at perihelion, the cloud condensation level

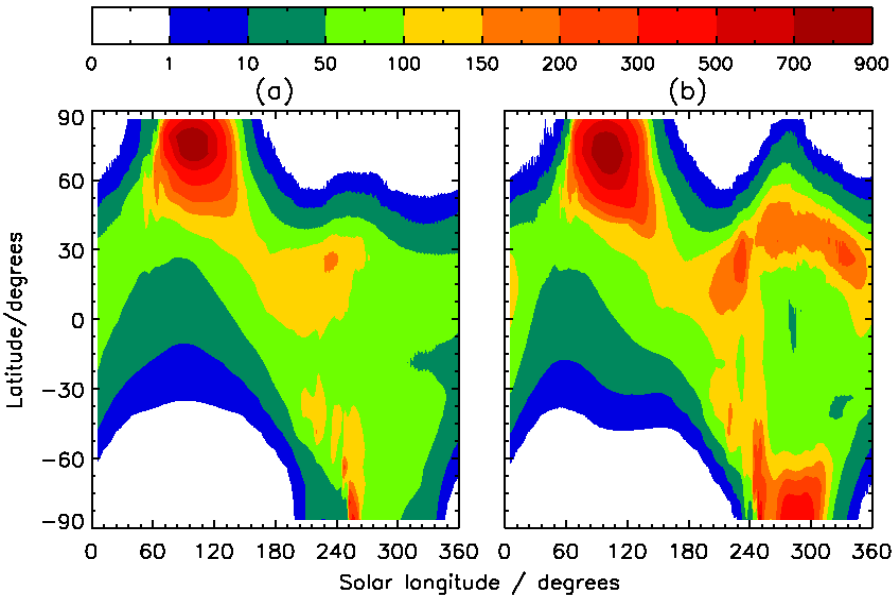

Figure 6.2: The vapour cycle at 35° obliquity (in prμm), using a present-day dust loading (a) and one more appropriate to the orbital parameters (b). Absolute vapour amounts are probably overestimated due to the overly large polar source used.

over the equator is at an altitude of around 35 km, slightly lower than at present due to higher humidity bringing saturation down to warmer altitudes. However, due to the higher vapour holding capacity of the (warmer) atmosphere when 35° opacity is used, cloud height rises to 50 km, allowing water vapour full use of the Hadley cell and thus allowing it to permeate further into the northern hemisphere. In addition, circulation is stronger for the 35° dust opacity, due to atmospheric heating caused by the extra dust loading. The enhanced cross-equatorial transport can be seen through the higher vapour amounts at 30°N during southern summer (see Figure 6.2 (b)). The reduced cap-size simulation gives a drier annual cycle, so saturation heights rise higher again by several km.

Madeleine et al. [2009] find that for a 'dusty' 35° climate, perihelion cloud level in fact stays lower than at present, at around 15 km. They use mid-latitude glaciers, rather than a north polar cap, as the water source, resulting in more annual sublimation and thus a much wetter atmosphere. The use of the north cap source here nonetheless gives agreement with their observation of perihelion vapour maxima at 50°S and 30°N, and cloud formation below 10 km at 30°N.

Notably, the fraction of atmospheric water that exists in the form of clouds is increased greatly in comparison to the present-day situation, as the wetter atmosphere more readily becomes saturated, even when heated by increased dust loading. Cloud mass accounts for around half the atmospheric water budget on average, as opposed to about a third at 25° obliquity. Figure 6.3 shows the

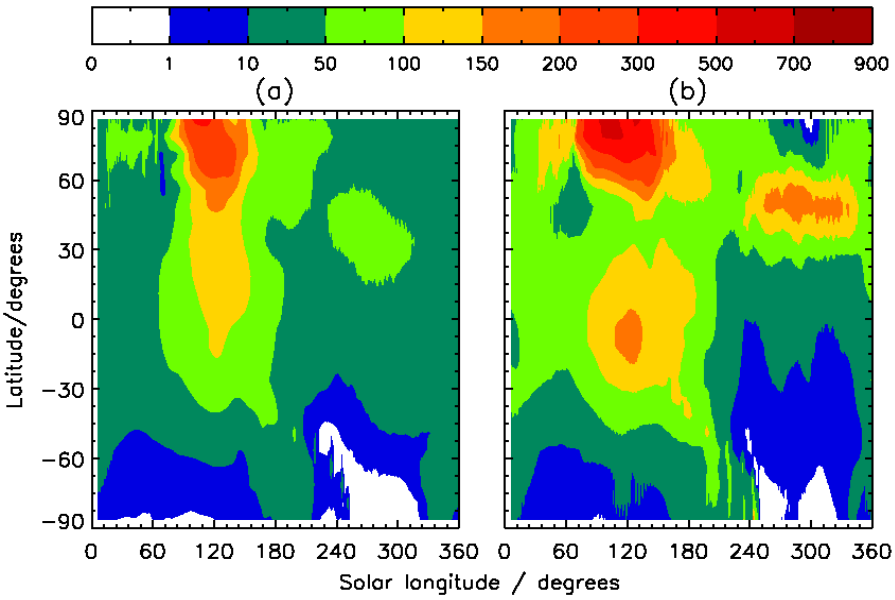

Figure 6.3: Cloud ice abundances (in prμm) at 35° obliquity, again for present-day dust loading (a) and 35° loading (b). As above, amounts are likely to be overestimates.

change in cloud abundance expected when using a realistic dust loading, rather than the one that exists currently — namely an increase in north polar hood cloud, as well as increases in the aphelion belt and over the subliming southern cap. Absolute abundances from the simulation using a smaller northern cap are probably more reliable however (bearing in mind also the limitations of the bulk cloud scheme used at present), and these are shown in Figure 6.4 (note the different contour levels to those in Figure 5.2).

This highlights the need to account for the radiative effects of ice clouds when simulating increased-obliquity climates. Cloud opacity for the present-day is currently overestimated by the MGCM, so the very large visible optical depths predicted for much of the year (often 10 or greater) should be treated with caution. Nevertheless, cloud visible opacity may well become comparable to the opacity due to dust in the aphelion belt or the north polar hood (since the order of magnitude increase in cloud thickness is accompanied by only a factor 2 or 3 increase in dust opacity), and so neglecting the radiative effects of clouds misses out a significant contribution to the atmospheric optical depth. This is particularly undesirable given the potential feedback effect of localised cooling just above the cloud layer allowing further cloud formation.

With annual insolation becoming more focussed on the polar regions, lower latitudes are then more favourable for surface ice formation, with the seasonal caps now extending to around 15° latitude in both hemispheres. The zonal heterogeneity seen in Figure 6.5 seems to be due to availability of precipitat-

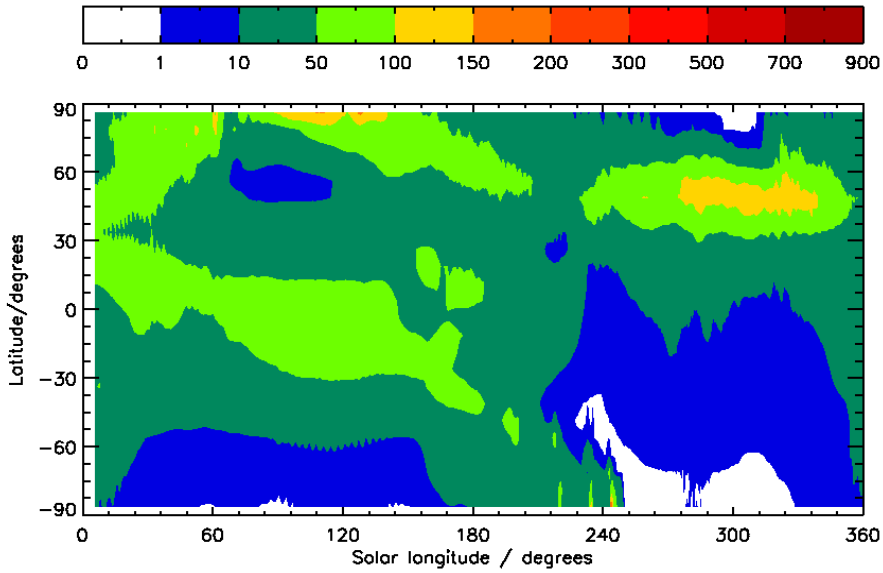

Figure 6.4: Column cloud abundance, in prμm, for the smaller cap/wet regolith 35° simulation.

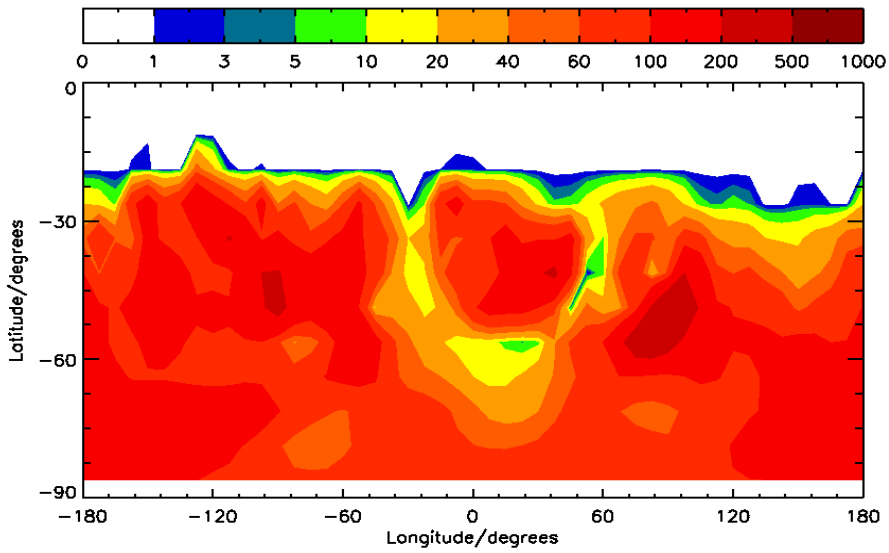

Figure 6.5: Surface ice thickness (in μm) for the seasonal south polar cap at $L_s = 90°$ (winter solstice), using the appropriate optical depth function for 35°.

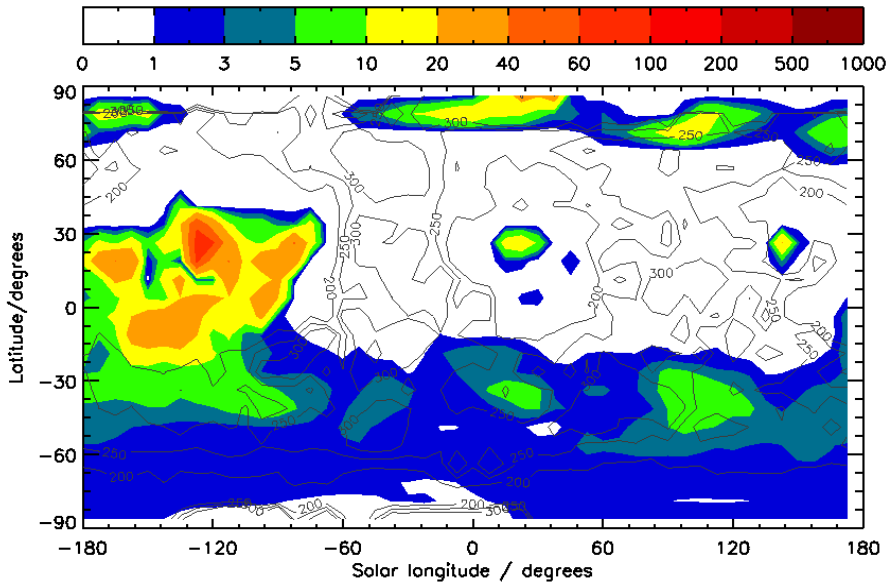

Figure 6.6: Column integrated subsurface ice (in μm) at $L_s = 90°$, using the appropriate optical depth function for 35°. Surface thermal inertia is overlaid (SI units of J m^{-2} K^{-1} s−1/2). Ice forms primarily in low thermal inertia regions.

ing cloud ice, as determined by southern hemisphere flow patterns. Mischna et al. [2003] found that the seasonal caps extend equatorward over ten model years, and that surface ice eventually becomes annually stable in certain longitude regions at latitudes of around 60°N. None of the simulations here show signs (within five years) of equatorward cap growth or perennial surface deposit formation — water instead enters the regolith, where it does become annually stable.

Ice deposits in the north polar regolith are maintained through northern summer, allowing an overall build-up. Ice density and accumulation rate are higher than at 25°, reflecting the increased overall wetness of the cycle. Perennial subsurface ice deposits also develop between 10°S and 30°N, most notably at longitudes 120°W–180°W (the Tharsis region), whereas south polar regolith ice is limited to the winter season. There is evidence in the northern low-latitudes for preferential formation in areas of low thermal inertia, which applies as heat does not diffuse efficiently down into the soil in these regions, keeping the subsurface cool. The indication is that equatorial deposits will build up with a distribution similar to that observed by Mars Odyssey (Figure 2.4). Overall subsurface ice formation is enhanced by the use of the 35° optical depth, due to lower mean global surface temperature. Subsurface ice at southern winter solstice is shown in Figure 6.6, for the derived 35° opacity.

6.3 Reversed perihelion

When northern summer is phased with perihelion, increased north polar summer insolation causes an increase in the northern polar maximum (Figure 6.7). It reaches a value similar to that seen at 35°, at around 900 prμm for an oversized polar cap, or ∼300 prμm for the realistic cap size with a wet polar regolith. The south polar maximum is much lower than this at 30–50 prμm in both cases. Clouds are much more ubiquitous than at present, with around 20 prμm (when using the smaller cap) in northern low-latitudes at $L_s = 180°$ (peaking later than at present, since the warmer northern summer atmosphere is not so easily saturated by cap sublimation). Thicker cloud is seen over the subliming south polar cap, and at the north pole at the beginning of winter — north polar hood cloud is not greatly different to the present-day during $L_s = 240°$–$360°$, as vapour transport from the southern hemisphere at this time is reduced (as explained below). The north polar seasonal water ice cap now extends further equatorward than the southern cap, since northern winter now coincides with aphelion so is longer and colder than southern winter.

The reversed perihelion simulation offers a chance to compare the now-competing effects of the topographic asymmetry and the Clancy effect — the former favours vapour transport back to the northern hemisphere, in all orbital configurations, whereas the latter, with the perihelion summer season now occurring in the northern hemisphere, would seem to predict a net southward movement of water.

With the present-day MGS dust distribution, increased dust heating occurs in the aphelion (southern summer) season, reducing the difference in vapour holding capacities between the two summer hemispheres, and thus inhibiting somewhat the cross-equatorial water transfer brought about by the Clancy effect. However, as shown in Figure 6.8, the southern polar cap does build up year-on-year, with accumulation rates of 100–300 μm per year poleward of 80°S. Subsurface ice also builds up at the south pole, at a rate of around 100 μm yr^{-1} within 75°–85°. Ice deposits begin to survive through southern summer by the fourth year of the run. The north polar regolith gains ice year-on-year as well, at rates of as much as 1 mm yr^{-1} poleward of 70°N. Seasonal ice deposits in northern winter extend to the equator, with a preference again seen for areas with low thermal inertia.

As shown previously, the actual dust opacity distribution for a reversed perihelion climate is likely to be much more uniform throughout the year, with the increased (decreased) insolation during perihelion (aphelion) season then allowing northern summer to dominate over southern summer with regard to moving water across the equator. The elevated saturation level at perihelion, compared to that at aphelion, can be seen in Figure 6.9. Using an Odyssey-like regolith and reduced polar cap size gives a drier annual cycle and thus saturation levels are raised further, allowing slightly greater Hadley-cell transport at both aphelion and perihelion. The combination of these two considerations leads to the large column vapour amounts seen in the southern hemisphere during southern winter, in Figure 6.7.

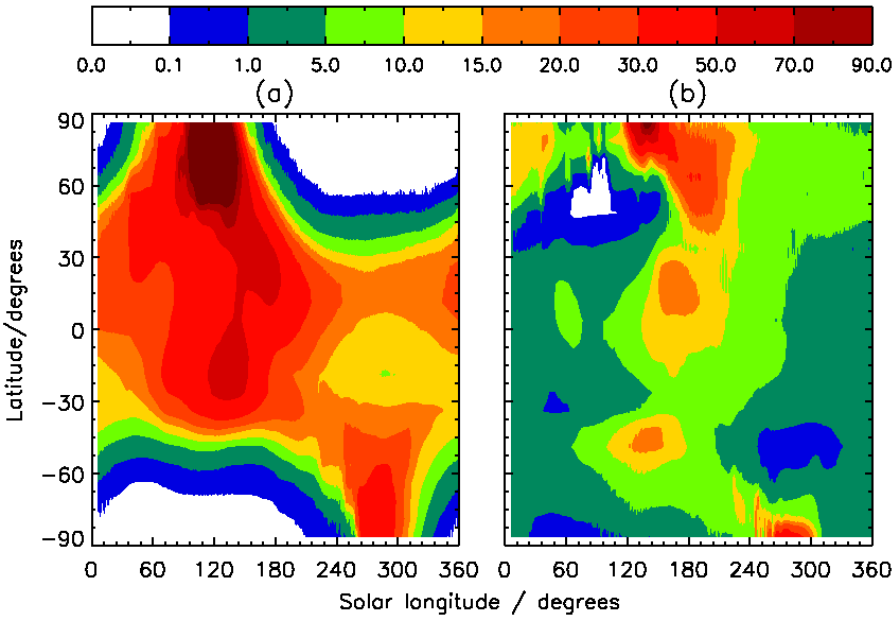

Figure 6.7: Zonal mean water vapour (a) and cloud ice (b) column abundances for reversed perihelion (same scale as Figure 5.2). A realistic cap size, initially wet polar regolith, and appropriate dust loading were used.

However, unlike the increased cap accumulation rate found by Montmessin et al. [2007], in this experiment the south polar cap does not build up annually with this dust loading. No perennial south polar deposits are formed, either on the surface or in the regolith. The reason for this is the 5–10 K southern summer pole surface temperature increase seen with the derived dust loading over the MGS case, due to the decreased southern summer opacity, particularly over the south pole. Warmer ground temperatures also lead to more adsorbed water in the south polar regolith, as opposed to water ice.

To investigate the sensitivity of cap formation and cross-equatorial transport to precise levels of dust loading, the run was repeated with the visible optical depth increased by 50%. As expected, greater atmospheric warming pushes saturation several kilometres higher, but the southern cap again fails to form. The crucial factor here is the opacity over the southern summer pole, as a certain level of dust in the atmosphere is required to cool the polar surface temperature sufficiently to allow ice to survive through summer. The dust-transporting UKMGCM predicts a relatively dust-free south polar region for this orbital scenario, therefore making it difficult for a southern cap to accumulate. This may be a flaw in the dust model prediction though, rather than a definitive denial of north-south polar ice transfer during times of reversed perihelion. It seems likely that, were the visible opacity over the south pole increased to ∼0.2

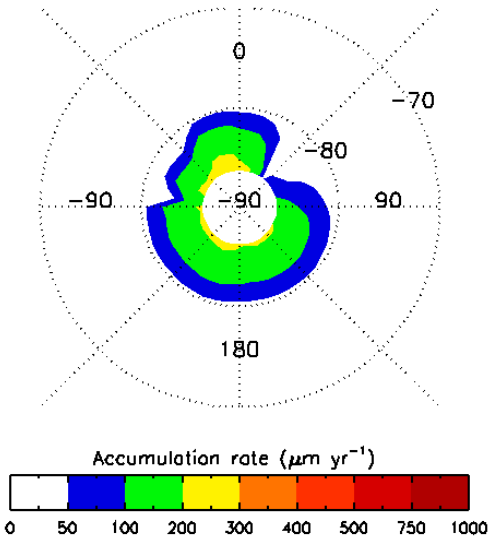

Figure 6.8: Annual gain in surface ice at the south pole, using the 'MGS' opacity distribution.

(the lower value used by Montmessin et al. [2007]) or more during summer, enhanced accumulation would be found, as a result of the greater net southward transport allowed by reversed perihelion dust loading, compared to present-day dust levels.

Alternatively, increasing the albedo of water ice deposits to 0.6 (modelling a very clear, dust-free precipitate), while keeping the opacity function as it was, does result in cap formation, with accumulation rates of up to 400 μm yr^{-1} measured. The cap also extends further from the south pole in this case.

The question of which hemisphere experiences a net gain is difficult to answer when using the northern cap as a water source, since inevitably the southern hemisphere regolith will absorb some water supplied from the northern source. The problem is that the atmosphere and subsurface have not reached equilibrium, so vapour will continue to sublimate from the north cap and fill the regolith on both sides of the equator, potentially for many model years.

What is clear is that southern cap build-up, rather than simply relying on a north-south annual water transfer, depends on several factors (at least, in the absence of any permanent CO_2 ice 'cold trap'), including surface temperatures (which are affected by dust loading and ice cloud amounts) and albedo of surface deposits (determined by the dust content of the polar atmosphere). The presence of the regolith further complicates matters, since water transported into the southern hemisphere during southern winter/spring may adsorb into the regolith rather than travelling to the cap and forming ice deposits.

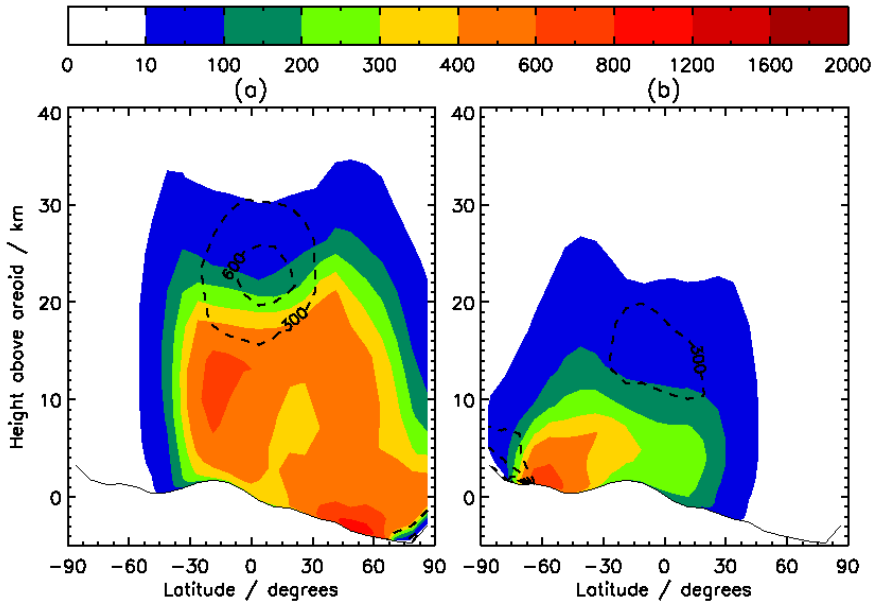

Figure 6.9: Water vapour (coloured contours, in 10^{-6} kg/kg) and ice cloud (dotted contours, same units) zonal mean distribution at perihelion (a) and aphelion (b) for the derived dust scenario at reversed perihelion (with an initially dry regolith). With the higher saturation level of around 25 km at perihelion, vapour can be effectively moved into the southern hemisphere, but the reverse flow at aphelion is limited by the ∼15 km cloud level. Saturation heights at perihelion/aphelion are closer together when the MGS dust distribution is used.

6.4 Low obliquity

With permanent CO_2 caps fixing polar surface temperatures at ∼140 K, a north polar source will not be able to supply vapour to the atmosphere, at 15° obliquity. Any other surface sources are unlikely — while mid-latitude glaciation can occur at higher obliquity [Madeleine et al., 2009], ice deposits do not survive the return to current obliquity, let alone a further reduction.

Provided the regolith contains water equatorward of the permanent cap edges, it can act as the source for the atmosphere. Humidity at 15° was thus found to be strongly dependent on how much water is placed in the subsurface initially. The holding capacity of the non-polar atmosphere is reduced from present-day though, due to the lower global pressure, and Pollack and Toon [1982] predict that deposition onto the permanent polar caps will reduce atmospheric vapour abundance by several orders of magnitude from its current level (however, they expected a lower global pressure than is found by the MGCM).

Two Odyssey-like regolith distributions were used — one with water amounts on the order of a few kg m^{-3} in each polar subsurface gridbox, and the other

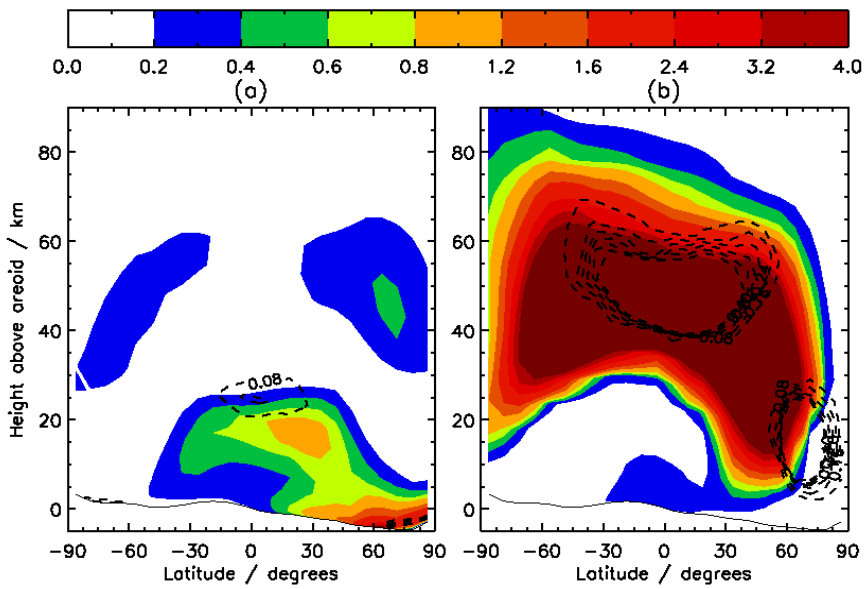

Figure 6.10: Aphelion (a) and perihelion (b) zonal mean water vapour (coloured contours, in 10^{-6} kg/kg) and ice cloud (dotted contours, same units) at 15° obliquity, showing the raised condensation levels (for the drier of the two regolith initialisations).

with these values multiplied by a factor of ten (similar to the initial regolith form used in 5.2). As expected, the resulting atmospheric humidities differ by roughly an order of magnitude. Northern summer maxima of 0.5 and 5 prμm are observed for the drier and wetter subsurface cases respectively, while a southern peak is not as clearly defined as it is currently.

With low global humidity, the height of saturation rises higher in the atmosphere. At aphelion, (relatively) significant amounts of vapour reach as high as 60 km into the mid-latitude atmosphere of each hemisphere. Thin equatorial clouds form at around 25 km altitude for the drier regolith (Figure 6.10), or 20 km in the wetter case. At perihelion, however, cloud level rises to 50 (42) km for the initially drier (wetter) subsurface, which, as explained already, enables large amounts of vapour to be transported far into the northern hemisphere by the mean circulation (particularly in the drier atmosphere case), making it much the wetter hemisphere throughout the entire year. North polar hood cloud forms at an increased altitude from the present-day predicted height ($\sim$15 km for the drier case), due to greater-than-saturation amounts of vapour being carried poleward in the descending Hadley branch.

The effect of using the lower, more realistic dust opacity (of Figure 5.3 (c)) is to reduce south-to-north transport at perihelion, due to a weaker circulation, slightly lower equatorial cloud ($\sim$45 km for the drier case), and a 25 km cloud layer that forms over the south pole (Figure 6.11). This results in lower vapour

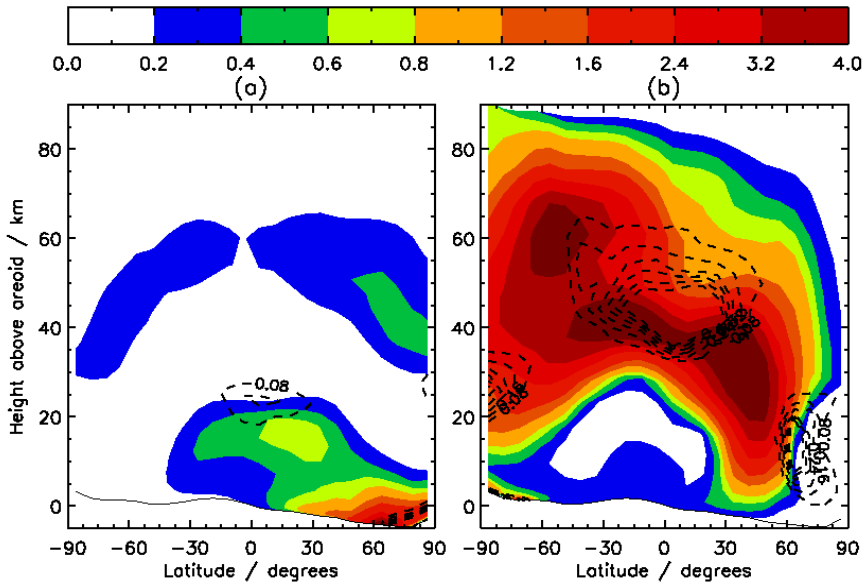

Figure 6.11: Aphelion (a) and perihelion (b) water vapour and ice cloud, as in Figure 6.10, but using a 15° dust loading. Northward perihelion transport is inhibited in comparison to Figure 6.10 (b).

amounts in the northern winter mid-latitudes, and reduced north polar hood cloud. Higher surface temperatures also lead to the development of a southern summer vapour peak at ∼70°S due to regolith desorption.

When the wetter initial subsurface is used, water is deposited onto the north polar cap (at around 50 μm yr^{-1}) an order of magnitude more rapidly than onto the southern cap; however, in the drier regolith simulation, no north cap deposition was observed, while southern cap accumulation does occur, albeit very slowly (<0.05 μm yr^{-1}, though using the 15° opacity function doubles this rate, presumably helped by the cloud layer that forms at the south pole in summer). The lack of north polar accumulation in the low-humidity case is surprising, since the north pole should be favoured both dynamically and thermodynamically for ice formation; further years' simulation may be required.

Water is lost from the equatorward edges of the initial regolith distribution (that is, 60°–75° in each hemisphere). Most desorption initially occurs in the northern hemisphere at L_s = 60°–120°, but after several years the southern hemisphere regolith begins to contribute also (as it takes some time for adsorbed water to move upwards through the dry layer overlying the initial south polar deposits). The majority of this water is adsorbed back into the regolith at lower latitudes, preferentially in the (wetter) northern hemisphere, with southern hemisphere adsorption and polar cap deposition accounting for smaller fractions of the water budget.

This is probably not the behaviour of the system in the long-term, as regolith intake would be expected moreso at colder, higher latitudes where atmospheric holding capacity is lower. A run was carried out using a regolith initially containing water at low- and mid-latitudes only, and this did indeed show water moving into the polar regolith, with the northern hemisphere preferred perhaps due to a bias in transport direction or because northern summer (aphelion) temperatures are cooler. The annual vapour peak occurs at 20°N for this configuration, further illustrating the strong dependence on initial regolith loading.

6.5 Future improvements?

It is expected that some of the experiments carried out here will be returned to once the model has been updated, to more precisely predict the effects of changes in orbital parameters. Having dust transport running simultaneously alongside the water cycle will naturally improve the accuracy of the dust optical depth seen by the model radiative code, and the addition of a radiative cloud scheme would prompt interesting changes in the results of any high-obliquity runs.

Madeleine et al. [2009] found that allowing thermal inertia to increase when thick surface ice deposits are present has the effect of reducing diurnal temperature variation and promoting further ice deposition. A similar effect could be achieved through the presence of subsurface ice, possibly affecting surface ice stability at higher obliquity. A regolith scheme which allows soil thermal inertia to vary with ice content would then give an improved representation of any climate in which ice forms in the subsurface.

Rerunning the reversed perihelion experiment with dust scavenging activated would be particularly interesting since dust, as well as water vapour, should be to some extent constrained by the Clancy effect if (through scavenging) cloud level acts as a vertical cap on the dust distribution. Some prediction of the albedo of any polar ice deposits, inferred from the dust content of the precipitate, would also be desirable.

Chapter 7

Future work

7.1 Restructuring and validation of GCM transport code

The key task for the immediate future, on which work has already begun, is the adaptation of existing versions of the UKMGCM to allow simultaneous transport of dust and water, and concurrent simulation of the two cycles. An important consideration in the structuring of the new model will be to allow for easy insertion of other tracer types in the future, as and when desired.

The initial step in producing the multiple-tracer code, which will be implemented in collaboration with other members of the UKMGCM group, is simply to alter the model code to handle multiple 'generalised' tracers. These will be advected by the existing semi-Lagrangian scheme and diffused vertically but will have no specific physics associated with them. The dust-transporting MGCM is already capable of following several different dust particle sizes at the same time, so this change should not be difficult to implement.

At this stage, however, it will be necessary to test the advection scheme to ensure it is working correctly and, in particular, conserving tracer mass satisfactorily. The tracer scheme and associated physics have yet to be formally checked since the move to the Linux platform, and the generalised transport system is likely to experience the same porting problems that were seen in the water scheme. However, since the water-transporting model is now working satisfactorily on Linux, solutions to these problems are largely already known. Some simple tests will be performed in order to check that tracers follow the circulation as expected, and do so independently of one another.

Mass conservation may still be an area of concern, seemingly for reasons related to model precision. It is proposed, within the group, that the model could soon be upgraded to store field values to twice the precision than is currently the case. This is now (in contrast to the early stages of the UKMGCM's development) well within the limits of available memory and computer power, and is likely to remove any remaining conservation problems, within the theoretical

limits of the advection scheme itself.

With this model framework in place, the dust and water physics schemes can be applied, enabling transport of 'real' tracer species. In particular, the system should be able to handle multiple dust particle sizes and one or more 'condensables', as well as other non-condensable gas species, such as methane or argon, that may be introduced to the model in the future. The only condensable tracer currently modelled is water vapour, but a sufficiently general tracer scheme will include the possibility of applying some of the water physics to carbon dioxide in future, to allow for the simulation of (among other phenomena) CO_2 clouds. Again, my experience with the water-transporting side of the code will be of great assistance at this point.

7.2 Incorporation and tuning of new physics

Another piece of work to be done in the coming months comes due to the proposed updating of the UKMGCM physics package. It is hoped that several modules from the LMD model, related to the water scheme, can be introduced into the UK code, to improve performance and to keep the two models in close alignment. In particular, a microphysical cloud scheme, from Montmessin et al. [2002], is now used in the LMD code, and will provide an improvement over the simple bulk cloud scheme used currently in the UKMGCM, with water ice density in the LMD scheme calculated as a function of atmospheric dust content. This aspect of the scheme will be particularly interesting when used within an explicitly dust-transporting model, which the UKMGCM should be by this stage (the LMD code currently, like the UK model, uses prescribed dust levels when simulating water transport).

On introducing the new routines into the UKMGCM, some 'tuning' of parameters will be necessary to produce realistic results, due to the differences in operation that do exist between the UK and French models. Successful incorporation into the UKMGCM of the new physics schemes will be necessary before any further development takes place.

The addition of radiative ice cloud effects, as noted already, is also of great importance should any higher obliquity simulations be carried out in future. The possibility of extending the GCM radiative scheme to include the effects of ice particles should be investigated.

At this point it will be beneficial to review again model output with respect to observations, and if appropriate, make changes to the regolith scheme (some as suggested by Böttger [2003]). As mentioned before (in 4.4.2), such alterations could include using a new set of isotherms for calculating adsorption, choosing to shut off atmospheric exchange in the presence of a layer of surface ice (CO_2 and/or water ice), and allowing soil thermal inertia to vary when subsurface ice is present. It is hoped that a combination of these alterations and/or the new physics package, together with an improved understanding of how model regolith initialisation translates into atmospheric vapour levels, will produce an annually-repeatable water cycle in better agreement with present observations

than is currently the case.

7.3 Modelling dust-water interactions

With transport of dust particles and water vapour/ice running simultaneously, the aim then is to couple the two cycles together, allowing interactions between the two tracers to affect the distributions of each. The microphysical scheme of Montmessin et al. [2002] already models a dependence of water ice cloud formation on the presence of dust particles, but without any direct feedback on dust levels. In reality, it is thought that by acting as condensation nuclei for cloud formation, dust particles experience an accelerated removal from the atmosphere due to their increased mass (when coated in ice) and hence their increased settling rate.

The combined effects of increased reflectance of dust particles when covered by ice, and their more rapid sedimentation, means that dust scavenging causes a net atmospheric cooling that is strongly non-linear [Rodin et al., 1999, Clancy et al., 1996]. Scavenging also suggests some confinement of dust to altitudes below that of vapour condensation, and the influence of water ice particles could affect dust vertical profiles on much shorter timescales than sedimentation or eddy mixing [Rodin et al., 1999].

One-dimensional modelling of dust-ice interactions has been carried out by Rodin et al. [1999] using a system which models the size distribution of dust particles, under the influence of water ice condensation and evaporation, through the method of moments, in which various quantities describing the dust distribution are held in successive power terms. Adapting this scheme to three dimensions for use in the UKMGCM may prove to be a desirable approach to take — one advantage is the method's consideration of dust and water ice mass conservation.

7.4 Project timeline

An approximate plan for the remaining two years of my project is as follows:

October 2009 Formulating and testing the generalised-transport code

November–December 2009 Adding the two tracer schemes; examining results from simultaneous dust and water transport

January–March 2010 (depending on availability of new code) Inserting and tuning the new LMD physics routines; adding ice clouds to the radiation scheme

October 2009–March 2010 Completing past-climate simulations, and writing up for a possible publication

January–May 2010 Re-evaluating regolith scheme operation and altering as required; constraining to observations in light of new routines available

June–September 2010 Investigating methods for parameterising dust particle scavenging

October 2010–May 2011 Coupling the UKMGCM dust and water cycles through scavenging interactions

June–September 2011 Revisiting past-climate simulations, now with coupled dust and water transport

January–September 2011 Write-up of thesis

Bibliography

V. R. Baker. Water and the martian landscape. *Nature*, 412:228–236, July 2001.

E. S. Barker, R. A. Schorn, A. Woszczyk, R. G. Tull, and S. J. Little. Mars: Detection of Atmospheric Water Vapor during the Southern Hemisphere Spring and Summer Season. *Science*, 170:1308–1310, December 1970.

H. M. Böttger. *Modelling the water cycle on Mars*. PhD thesis, University of Oxford, 2003.

H. M. Böttger, S. R. Lewis, P. L. Read, and F. Forget. The effects of the martian regolith on GCM water cycle simulations. *Icarus*, 177:174–189, September 2005. doi: 10.1016/j.icarus.2005.02.024.

W. V. Boynton, W. C. Feldman, S. W. Squyres, T. H. Prettyman, J. Brückner, L. G. Evans, R. C. Reedy, R. Starr, J. R. Arnold, D. M. Drake, P. A. J. Englert, A. E. Metzger, I. Mitrofanov, J. I. Trombka, C. d'Uston, H. Wänke, O. Gasnault, D. K. Hamara, D. M. Janes, R. L. Marcialis, S. Maurice, I. Mikheeva, G. J. Taylor, R. Tokar, and C. Shinohara. Distribution of Hydrogen in the Near Surface of Mars: Evidence for Subsurface Ice Deposits. *Science*, 297:81–85, July 2002. doi: 10.1126/science.1073722.

R. T. Clancy and S. W. Lee. A new look at dust and clouds in the Mars atmosphere - Analysis of emission-phase-function sequences from global Viking IRTM observations. *Icarus*, 93:135–158, September 1991. doi: 10.1016/0019-1035(91)90169-T.

R. T. Clancy, A. W. Grossman, M. J. Wolff, P. B. James, D. J. Rudy, Y. N. Billawala, B. J. Sandor, S. W. Lee, and D. O. Muhleman. Water vapor saturation at low altitudes around Mars aphelion: A key to Mars climate? *Icarus*, 122:36–62, July 1996. doi: 10.1006/icar.1996.0108.

S. M. Clifford. A model for the hydrologic and climatic behavior of water on Mars. *J. Geophys. Res.*, 98:10973–+, June 1993. doi: 10.1029/93JE00225.

A. Colaprete and O. B. Toon. The radiative effects of martian water ice clouds on the local atmospheric temperature profile. *Icarus*, 145:524–532, June 2000. doi: 10.1006/icar.2000.6364.

M. Collins, S. R. Lewis, and P. L. Read. Gravity wave drag in a global circulation model of the martian atmosphere: parameterisation and validation. *Adv. Space Res.*, 19:1245–1254, May 1997. doi: 10.1016/S0273-1177(97)00277-9.

J. A. Cutts and B. H. Lewis. Models of climate cycles recorded in Martian polar layered deposits. *Icarus*, 50:216–244, June 1982. doi: 10.1016/0019-1035(82)90124-5.

F. P. Fanale and J. R. Salvail. Quasi-periodic atmosphere-regolith-cap CO2 redistribution in the martian past. *Icarus*, 111:305–316, October 1994. doi: 10.1006/icar.1994.1147.

C. B. Farmer and P. E. Doms. Global seasonal variation of water vapor on Mars and the implications of permafrost. *J. Geophys. Res.*, 84:2881–2888, June 1979. doi: 10.1029/JB084iB06p02881.

A. A. Fedorova, A. V. Rodin, and I. V. Baklanova. MAWD observations revisited: seasonal behavior of water vapor in the martian atmosphere. *Icarus*, 171:54–67, September 2004. doi: 10.1016/j.icarus.2004.04.017.

W. C. Feldman, T. H. Prettyman, W. V. Boynton, J. R. Murphy, S. Squyres, S. Karunatillake, S. Maurice, R. L. Tokar, G. W. McKinney, D. K. Hamara, N. Kelly, and K. Kerry. CO_2 frost cap thickness on Mars during northern winter and spring. *J. Geophys. Res. (Planets)*, 108:5103–+, September 2003. doi: 10.1029/2003JE002101.

L. K. Fenton, P. E. Geissler, and R. M. Haberle. Global warming and climate forcing by recent albedo changes on Mars. *Nature*, 446:646–649, April 2007. doi: 10.1038/nature05718.

F. Forget. Improved optical properties of the Martian atmospheric dust for radiative transfer calculations in the infrared. *Geophys. Res. Lett.*, 25:1105–1108, April 1998. doi: 10.1029/98GL50653.

F. Forget, F. Hourdin, R. Fournier, C. Hourdin, O. Talagrand, M. Collins, S. R. Lewis, P. L. Read, and J.-P. Huot. Improved general circulation models of the Martian atmosphere from the surface to above 80 km. *J. Geophys. Res.*, 104:24155–24176, October 1999. doi: 10.1029/1999JE001025.

F. Forget, R. M. Haberle, F. Montmessin, B. Levrard, and J. W. Head. Formation of Glaciers on Mars by Atmospheric Precipitation at High Obliquity. *Science*, 311:368–371, January 2006. doi: 10.1126/science.1120335.

V. Formisano, F. Angrilli, G. Arnold, S. Atreya, G. Bianchini, D. Biondi, A. Blanco, M. I. Blecka, A. Coradini, L. Colangeli, A. Ekonomov, F. Esposito, S. Fonti, M. Giuranna, D. Grassi, V. Gnedykh, A. Grigoriev, G. Hansen, H. Hirsh, I. Khatuntsev, A. Kiselev, N. Ignatiev, A. Jurewicz, E. Lellouch, J. Lopez Moreno, A. Marten, A. Mattana, A. Maturilli, E. Mencarelli, M. Michalska, V. Moroz, B. Moshkin, F. Nespoli, Y. Nikolsky,

R. Orfei, P. Orleanski, V. Orofino, E. Palomba, D. Patsaev, G. Piccioni, M. Rataj, R. Rodrigo, J. Rodriguez, M. Rossi, B. Saggin, D. Titov, and L. Zasova. The Planetary Fourier Spectrometer (PFS) onboard the European Mars Express mission. *Planet. Space Sci.*, 53:963–974, August 2005. doi: 10.1016/j.pss.2004.12.006.

T. Fouchet, E. Lellouch, N. I. Ignatiev, F. Forget, D. V. Titov, M. Tschimmel, F. Montmessin, V. Formisano, M. Giuranna, A. Maturilli, and T. Encrenaz. Martian water vapor: Mars Express PFS/LW observations. *Icarus*, 190:32–49, September 2007. doi: 10.1016/j.icarus.2007.03.003.

R. M. Haberle and B. M. Jakosky. Sublimation and transport of water from the north residual polar CAP on Mars. *J. Geophys. Res.*, 95:1423–1437, February 1990. doi: 10.1029/JB095iB02p01423.

R. M. Haberle, J. B. Pollack, J. R. Barnes, R. W. Zurek, C. B. Leovy, J. R. Murphy, H. Lee, and J. Schaeffer. Mars atmospheric dynamics as simulated by the NASA AMES General Circulation Model. I - The zonal-mean circulation. *J. Geophys. Res.*, 98:3093–3123, February 1993. doi: 10.1029/92JE02946.

R. M. Haberle, C. P. McKay, J. Schaeffer, N. A. Cabrol, E. A. Grin, A. P. Zent, and R. Quinn. On the possibility of liquid water on present-day Mars. *J. Geophys. Res.*, 106:23317–23326, October 2001. doi: 10.1029/2000JE001360.

R. M. Haberle, J. R. Murphy, and J. Schaeffer. Orbital change experiments with a Mars general circulation model. *Icarus*, 161:66–89, January 2003. doi: 10.1016/S0019-1035(02)00017-9.

J. W. Head, J. F. Mustard, M. A. Kreslavsky, R. E. Milliken, and D. R. Marchant. Recent ice ages on Mars. *Nature*, 426:797–802, December 2003.

J. W. Head, III, H. Hiesinger, M. A. Ivanov, M. A. Kreslavsky, S. Pratt, and B. J. Thomson. Possible ancient oceans on Mars: evidence from Mars Orbiter Laser Altimeter data. *Science*, 286:2134–2137, December 1999. doi: 10.1126/science.286.5447.2134.

D. P. Hinson, G. L. Tyler, J. L. Hollingsworth, and R. J. Wilson. Radio occultation measurements of forced atmospheric waves on Mars. *J. Geophys. Res.*, 106:1463–1480, January 2001. doi: 10.1029/2000JE001291.

D. P. Hinson, M. Pätzold, S. Tellmann, B. Häusler, and G. L. Tyler. The depth of the convective boundary layer on Mars. *Icarus*, 198:57–66, November 2008. doi: 10.1016/j.icarus.2008.07.003.

B. J. Hoskins and A. J. Simmons. A multi-layer spectral model and the semi-implicit method. *Quart. J. R. Meteor. Soc.*, 101:637–655, 1975.

F. Hourdin. A new representation of the absorption by the CO2 15-microns band for a Martian general circulation model. *J. Geophys. Res.*, 97:18319–+, November 1992.

B. M. Jakosky. The seasonal cycle of water on Mars. *Space Sci. Rev.*, 41: 131–200, June 1985. doi: 10.1007/BF00241348.

B. M. Jakosky and C. B. Farmer. The seasonal and global behavior of water vapor in the Mars atmosphere - Complete global results of the Viking atmospheric water detector experiment. *J. Geophys. Res.*, 87:2999–3019, April 1982. doi: 10.1029/JB087iB04p02999.

B. M. Jakosky and R. M. Haberle. Year-to-year instability of the Mars south polar CAP. *J. Geophys. Res.*, 95:1359–1365, February 1990. doi: 10.1029/JB095iB02p01359.

H. H. Kieffer, T. Z. Martin, S. C. Chase, Jr., E. D. Miner, and F. D. Palluconi. Martian north pole summer temperatures - Dirty water ice. *Science*, 194: 1341–1344, December 1976. doi: 10.1126/science.194.4271.1341.

J. Laskar and P. Robutel. The chaotic obliquity of the planets. *Nature*, 361: 608–612, February 1993. doi: 10.1038/361608a0.

J. Laskar, A. C. M. Correia, M. Gastineau, F. Joutel, B. Levrard, and P. Robutel. Long term evolution and chaotic diffusion of the insolation quantities of Mars. *Icarus*, 170:343–364, August 2004. doi: 10.1016/j.icarus.2004.04.005.

C. Leovy. Weather and climate on Mars. *Nature*, 412:245–249, July 2001.

C. Leovy and Y. Mintz. Numerical Simulation of the Atmospheric Circulation and Climate of Mars. *J. Atmos. Sci.*, 26:1167–1190, November 1969. doi: 10.1175/1520-0469(1969)026.

S. R. Lewis and P. L. Read. Equatorial jets in the dusty Martian atmosphere. *J. Geophys. Res. (Planets)*, 108:5034–+, April 2003. doi: 10.1029/2002JE001933.

M. L. Litvak, I. G. Mitrofanov, A. S. Kozyrev, A. B. Sanin, V. I. Tretyakov, W. V. Boynton, D. Hamara, C. Shinohara, and R. S. Saunders. Modeling of Martian seasonal caps from HEND/ODYSSEY data. *Adv. Space Res.*, 36: 2156–2161, 2005. doi: 10.1016/j.asr.2005.09.007.

M. L. Litvak, I. G. Mitrofanov, A. S. Kozyrev, A. B. Sanin, V. I. Tretyakov, W. V. Boynton, N. J. Kelly, D. Hamara, C. Shinohara, and R. S. Saunders. Comparison between polar regions of Mars from HEND/Odyssey data. *Icarus*, 180:23–37, January 2006. doi: 10.1016/j.icarus.2005.08.009.

J.-B. Madeleine, F. Forget, James W. Head, B. Levrard, F. Montmessin, and E. Millour. Amazonian northern mid-latitude glaciation on mars: A proposed climate scenario. *Icarus*, In Press, Corrected Proof:–, 2009. ISSN 0019-1035. doi: DOI: 10.1016/j.icarus.2009.04.037.

J. A. Magalhães, J. T. Schofield, and A. Seiff. Results of the Mars Pathfinder atmospheric structure investigation. *J. Geophys. Res.*, 104:8943–8956, April 1999. doi: 10.1029/1998JE900041.

S. M. Metzger, J. R. Carr, J. R. Johnson, T. J. Parker, and M. T. Lemmon. Dust devil vortices seen by the Mars Pathfinder camera. *Geophys. Res. Lett.*, 26:2781–2784, September 1999. doi: 10.1029/1999GL008341.

S. M. Milkovich and J. W. Head. North polar cap of Mars: Polar layered deposit characterization and identification of a fundamental climate signal. *J. Geophys. Res. (Planets)*, 110:1005–+, January 2005. doi: 10.1029/2004JE002349.

M. A. Mischna, M. I. Richardson, R. J. Wilson, and D. J. McCleese. On the orbital forcing of Martian water and CO_2 cycles: A general circulation model study with simplified volatile schemes. *J. Geophys. Res. (Planets)*, 108:5062–+, June 2003. doi: 10.1029/2003JE002051.

I. G. Mitrofanov, M. L. Litvak, A. S. Kozyrev, A. B. Sanin, V. I. Tret'yakov, V. Y. Grin'kov, W. V. Boynton, C. Shinohara, D. Hamara, and R. S. Saunders. Soil Water Content on Mars as Estimated from Neutron Measurements by the HEND Instrument Onboard the 2001 Mars Odyssey Spacecraft. *Solar Syst. Res.*, 38:253–257, July 2004. doi: 10.1023/B:SOLS.0000037461.70809.45.

F. Montmessin. The Orbital Forcing of Climate Changes on Mars. *Space Sci. Rev.*, 125:457–472, August 2006. doi: 10.1007/s11214-006-9078-x.

F. Montmessin, P. Rannou, and M. Cabane. New insights into Martian dust distribution and water-ice cloud microphysics. *J. Geophys. Res. (Planets)*, 107:5037–+, June 2002. doi: 10.1029/2001JE001520.

F. Montmessin, R. M. Haberle, F. Forget, Y. Langevin, R. T. Clancy, and J.-P. Bibring. On the origin of perennial water ice at the south pole of Mars: A precession-controlled mechanism? *J. Geophys. Res. (Planets)*, 112:8–+, August 2007. doi: 10.1029/2007JE002902.

B. C. Murray, L. A. Soderblom, J. A. Cutts, R. P. Sharp, D. J. Milton, and R. B. Leighton. Geological Framework of the South Polar Region of Mars (A 4. 4). *Icarus*, 17:328–+, October 1972. doi: 10.1016/0019-1035(72)90004-8.

J. F. Mustard, C. D. Cooper, and M. K. Rifkin. Evidence for recent climate change on Mars from the identification of youthful near-surface ground ice. *Nature*, 412:411–414, July 2001.

C. E. Newman, S. R. Lewis, P. L. Read, and F. Forget. Modeling the Martian dust cycle, 1. Representations of dust transport processes. *J. Geophys. Res. (Planets)*, 107:5123–+, December 2002. doi: 10.1029/2002JE001910.

C. E. Newman, S. R. Lewis, and P. L. Read. The atmospheric circulation and dust activity in different orbital epochs on Mars. *Icarus*, 174:135–160, March 2005. doi: 10.1016/j.icarus.2004.10.023.

D. A. Paige and A. P. Ingersoll. Annual heat balance of Martian polar caps - Viking observations. *Science*, 228:1160–1168, June 1985. doi: 10.1126/science.228.4704.1160.

T. J. Parker, D. S. Gorsline, R. S. Saunders, D. C. Pieri, and D. M. Schneeberger. Coastal geomorphology of the Martian northern plains. *J. Geophys. Res.*, 98: 11061–+, June 1993. doi: 10.1029/93JE00618.

J. J. Plaut, R. Kahn, E. A. Guinness, and R. E. Arvidson. Accumulation of sedimentary debris in the south polar region of Mars and implications for climate history. *Icarus*, 76:357–377, November 1988. doi: 10.1016/0019-1035(88)90076-0.

J. B. Pollack and O. B. Toon. Quasi-periodic climate changes on Mars - A review. *Icarus*, 50:259–287, June 1982. doi: 10.1016/0019-1035(82)90126-9.

A. Priestley. A Quasi-Conservative Version of the Semi-Lagrangian Advection Scheme. *Monthly Weather Rev.*, 121:621–629, 1993.

P. L. Read and S. R. Lewis. *The Martian Climate Revisited: Atmosphere and Environment of a Desert Planet*. Springer Praxis, 2004.

N. O. Rennó, A. A. Nash, J. Lunine, and J. Murphy. Martian and terrestrial dust devils: Test of a scaling theory using Pathfinder data. *J. Geophys. Res.*, 105:1859–1866, January 2000. doi: 10.1029/1999JE001037.

N. O. Renno, B. C. Clark, L. Drube, D. Fisher, W. Goetz, M. Hecht, H. U. Keller, S. Kounaves, M. Lemmon, M. B. Madsen, J. Marshall, M. Mehta, M. Mellon, M. Smith, P. H. Smith, C. Stoker, L. Tamppari, S. Wood, S. M. Young, and Z. Zent. Physical and Thermodynamical Evidence of Liquid Water on Mars. *LPI Contributions*, 1447:9127–+, November 2008.

M. I. Richardson and R. J. Wilson. A topographically forced asymmetry in the martian circulation and climate. *Nature*, 416:298–301, March 2002.

A. V. Rodin, O. I. Korablev, and V. I. Moroz. Vertical Distribution of Water in the Near-Equatorial Troposphere of Mars: Water Vapor and Clouds. *Icarus*, 125:212–229, January 1997. doi: 10.1006/icar.1996.5602.

A. V. Rodin, R. T. Clancy, and R. J. Wilson. Dynamical properties of Mars water ice clouds and their interactions with atmospheric dust and radiation. *Adv. Space Res.*, 23:1577–1585, 1999. doi: 10.1016/S0273-1177(99)00173-8.

C. Sagan and R. A. Bagnold. Fluid transport on earth and aeolian transport on Mars. *Icarus*, 26:209–218, October 1975. doi: 10.1016/0019-1035(75)90080-9.

D. E. Smith, M. T. Zuber, and G. A. Neumann. Seasonal Variations of Snow Depth on Mars. *Science*, 294:2141–2146, December 2001. doi: 10.1126/science.1066556.

M. D. Smith. The annual cycle of water vapor on Mars as observed by the Thermal Emission Spectrometer. *J. Geophys. Res. (Planets)*, 107:5115–+, November 2002. doi: 10.1029/2001JE001522.

M. D. Smith. Interannual variability in TES atmospheric observations of Mars during 1999-2003. *Icarus*, 167:148–165, January 2004. doi: 10.1016/S0019-1035(03)00287-2.

H. Spinrad, G. Münch, and L. D. Kaplan. Letter to the Editor: the Detection of Water Vapor on Mars. *Astrophysical Journal*, 137:1319–+, May 1963. doi: 10.1086/147613.

A. L. Sprague, D. M. Hunten, L. R. Doose, R. E. Hill, W. V. Boynton, M. D. Smith, and J. C. Pearl. Mars atmospheric water vapor abundance: 1991 1999, emphasis 1998 1999. *Icarus*, 184:372–400, October 2006. doi: 10.1016/j.icarus.2006.05.021.

D. V. Titov, W. J. Markiewicz, N. Thomas, H. U. Keller, R. M. Sablotny, M. G. Tomasko, M. T. Lemmon, and P. H. Smith. Measurements of the atmospheric water vapor on Mars by the Imager for Mars Pathfinder. *J. Geophys. Res.*, 104:9019–9026, April 1999. doi: 10.1029/1998JE900046.

T. N. Titus, H. H. Kieffer, and P. R. Christensen. Exposed Water Ice Discovered near the South Pole of Mars. *Science*, 299:1048–1051, February 2003. doi: 10.1126/science.1080497.

O. B. Toon, J. B. Pollack, and C. Sagan. Physical properties of the particles composing the Martian dust storm of 1971-1972. *Icarus*, 30:663–696, April 1977. doi: 10.1016/0019-1035(77)90088-4.

M. Tschimmel, N. I. Ignatiev, D. V. Titov, E. Lellouch, T. Fouchet, M. Giuranna, and V. Formisano. Investigation of water vapor on Mars with PFS/SW of Mars Express. *Icarus*, 195:557–575, June 2008. doi: 10.1016/j.icarus.2008.01.018.

W. R. Ward. Climatic variations on Mars. I. Astronomical theory of insolation. *J. Geophys. Res.*, 79:3375–3386, 1974. doi: 10.1029/JC079i024p03375.

B. R. White. Soil transport by winds on Mars. *J. Geophys. Res.*, 84:4643–4651, August 1979. doi: 10.1029/JB084iB09p04643.

J. A. Whiteway, L. Komguem, C. Dickinson, C. Cook, M. Illnicki, J. Seabrook, V. Popovici, T. J. Duck, R. Davy, P. A. Taylor, J. Pathak, D. Fisher, A. I. Carswell, M. Daly, V. Hipkin, A. P. Zent, M. H. Hecht, S. E. Wood, L. K. Tamppari, N. Renno, J. E. Moores, M. T. Lemmon, F. Daerden, and P. H. Smith. Mars Water-Ice Clouds and Precipitation. *Science*, 325:68–, July 2009. doi: 10.1126/science.1172344.

M. J. Wolff and R. T. Clancy. Constraints on the size of Martian aerosols from Thermal Emission Spectrometer observations. *J. Geophys. Res. (Planets)*, 108:5097–+, September 2003. doi: 10.1029/2003JE002057.

L. Zasova, V. Formisano, V. Moroz, D. Grassi, N. Ignatiev, M. Giuranna, G. Hansen, M. Blecka, A. Ekonomov, E. Lellouch, S. Fonti, A. Grigoriev, H. Hirsch, I. Khatuntsev, A. Mattana, A. Maturilli, B. Moshkin, D. Patsaev, G. Piccioni, M. Rataj, and B. Saggin. Water clouds and dust aerosols observations with PFS MEX at Mars. *Planet. Space Sci.*, 53:1065–1077, August 2005. doi: 10.1016/j.pss.2004.12.010.

A. P. Zent, R. M. Haberle, H. C. Houben, and B. M. Jakosky. A coupled subsurface-boundary layer model of water on Mars. *J. Geophys. Res.*, 98: 3319–3337, February 1993. doi: 10.1029/92JE02805.

M. T. Zuber, D. E. Smith, S. C. Solomon, J. B. Abshire, R. S. Afzal, O. Aharonson, K. Fishbaugh, P. G. Ford, H. V. Frey, J. B. Garvin, J. W. Head, A. B. Ivanov, C. L. Johnson, D. O. Muhleman, G. A. Neumann, G. H. Pettengill, R. J. Phillips, X. Sun, H. J. Zwally, W. B. Banerdt, and T. C. Duxbury. Observations of the North Polar Region of Mars from the Mars Orbiter Laser Altimeter. *Science*, 282:2053–+, December 1998. doi: 10.1126/science.282.5396.2053.

M. T. Zuber, S. C. Solomon, R. J. Phillips, D. E. Smith, G. L. Tyler, O. Aharonson, G. Balmino, W. B. Banerdt, J. W. Head, C. L. Johnson, F. G. Lemoine, P. J. McGovern, G. A. Neumann, D. D. Rowlands, and S. Zhong. Internal Structure and Early Thermal Evolution of Mars from Mars Global Surveyor Topography and Gravity. *Science*, 287:1788–1793, March 2000. doi: 10.1126/science.287.5459.1788.